CHARACTERIZATION OF THE VELOCITY PROFILE IN THE TEST SECTION IN A SUBSONIC WIND TUNNEL

Presented by:

Author: Alejandro Patiño Molano
alejandro.patino.molano@correounivalle.edu.co

Director: Guillermo Andrés Jaramillo Pizarro Ph.D.
guillermo.jaramillo@correounivalle.edu.co

A Thesis to apply for a degree of Bachelor of Science in
Mechanical Engineering



IMPETUS INDOMITUS
Research Team in energy conversion and propulsion revolution
School of Mechanical Engineering
Universidad del Valle
December 9, 2024

Acknowledgments

First and foremost, I would like to express my gratitude to God for giving me the opportunity to pursue my education and complete my undergraduate degree. His guidance and strength have been invaluable throughout this journey, providing me with the perseverance and clarity needed to overcome challenges and achieve this significant milestone.

I am deeply thankful to my family for their support, encouragement, and patience during the development of this work. Their love and understanding have been a constant source of motivation, and their belief in my abilities has pushed me to give my very best every step of the way.

I extend my heartfelt thanks to Professor Guillermo and the IMPETUS INDOMITUS team for their support and the resources they provided, which were essential for the successful completion of this project. Their guidance, technical expertise, and collaborative spirit enriched my learning experience and contributed greatly to the quality of this work.

To my fellow university classmates, I owe a special thanks for their timely assistance and willingness to share knowledge whenever I sought their help, be it in technical concepts or in practical aspects of construction. I am grateful for the sense of community they fostered.

Abstract

This work presents the development of a modular, open-circuit subsonic wind tunnel, 3D-printed and designed for characterizing the velocity profile in its test section. A simple yet detailed design process was followed to ensure reproducibility. Although the wind tunnel currently operates at speeds up to 23.50 m/s, it can reach up to 40.00 m/s by replacing the fan. Designed within the IMPETUS INDOMITUS team, this wind tunnel has a test section with dimensions of 25x25x70 cm, enabling a wider range of aerodynamic experiments. A comparison was conducted between experimental velocity profiles and those obtained through Computational Fluid Dynamics (CFD) simulations using OpenFoam at speeds of 5, 10, 15, and 20 m/s. These comparisons showed in the mid plane of the test section an average experimental velocity of $20{,}02 \pm 0{,}41e-4m/s$ and a simulated velocity of 20.28 m/s, with a maximum error of 4.85 %, thereby verifying the reliability of the computational results. Additionally, turbulence intensity measurements indicated a maximum value of $1{,}07 \pm 0{,}06e-6$ % at 20 m/s, confirming the suitability of this wind tunnel for aerodynamic research and development.

keywords: Wind tunnel, Turbulence Intensity, Velocity profile, OpenFoam, experimental, design, airflow

Index

Acknowledgments **2**

Abstract **3**

Figures Index **5**

Tables Index **7**

1. Introduction **10**
1.1. Contextual framework . . . 10
1.2. Problem statement . . . 11
1.3. Problem tree . . . 11
1.4. Literature review . . . 12
1.4.1. History . . . 12
1.4.2. Wind tunnels in Colombia . . . 14
1.4.3. State of the art . . . 15
1.5. Justification . . . 17
1.6. Objectives . . . 17
1.6.1. General objective . . . 17
1.6.2. Specific objectives . . . 18
1.6.3. Objectives tree . . . 18
1.7. Methodology . . . 18
1.8. Expected impact . . . 21

2. Theoretical framework **22**
2.1. Open circuit wind tunnel . . . 22
2.2. Open circuit wind tunnel sections . . . 23
2.2.1. Contraction section . . . 24
2.2.2. Test section . . . 25
2.2.3. Diffuser . . . 25
2.2.4. Honeycomb . . . 27
2.2.5. Screens . . . 28
2.2.6. Fan . . . 28
2.3. Pressure and Pressure loss . . . 29
2.4. Velocity Profile . . . 29

3.Design and Construction **31**
3.1. Thickness Calculations . . . 33
3.2. Materials . . . 34
3.3. Fan Parameters . . . 35
3.4. Test Section . . . 36
3.4.1. Pressure losses in Test Section . . . 37
3.5. Honeycomb . . . 37
3.5.1. Pressure losses in Honeycomb . . . 38
3.6. Contraction zone . . . 39
3.6.1. Pressure losses in the contraction zone . . . 39
3.7. Diffuser . . . 40
3.7.1. Pressure losses in Diffuser . . . 41
3.8. Fan transition . . . 42
3.9. Theoretical Pressure losses . . . 43
3.10. Control Circuit . . . 44
3.11. Structure . . . 44
3.12. Wind Tunnel Assembly . . . 46

4.CFD Simulation **49**
4.1. Parameters for CFD Using OpenFoam . . . 49
4.2. Mesh Parameters . . . 51
4.3. OpenFOAM Parameters . . . 53
4.4. y+ parameter . . . 56

5. Data recompilation **58**
5.1. Experimental results . . . 58
5.1.1. Turbulent Intensity . . . 63
5.1.2. Experimental Pressure Losses . . . 65
5.2. Simulation results . . . 65
5.2.1. Pressure losses in simulation . . . 68
5.3. Uncertainty Analysis . . . 69
5.3.1. Velocity uncertainty analysis . . . 69
5.3.2. Turbulence Intensity uncertainty analysis . . . 69
5.4. Analysis of Results . . . 70

6. Conclusions **74**

7. Future Work **75**

References **76**

Figures Index

1.1. Problem tree diagram. Source: [Author] . . . 12
1.2. Wright brothers wind tunnel replica made in 1938. Source: [12] . . . 13
1.3. Small-scale academic wind tunnels used for research and educational purposes in different universities. Source [Author] . . . 14
1.4. First wind tunnel in Colombia. Source:[16] . . . 14
1.5. Plasma wind tunnel testing. Source: [18] . . . 16
1.6. Objectives tree diagram. Source: [Author] . . . 18
1.7. Project flow diagram. Source: [Author] . . . 19
2.8. Suck-down (top) wind tunnel and Blow-down (down) wind tunnel. Source:[Author] . 22
2.9. 5th Order polynomial contraction section side shape. Source: [Author] . . . 24
2.10. Test section length restriction Source: [Author] . . . 25
2.11. Three different diffuser geometries Source: [Author] . . . 26
2.12. Recommended design region for 2D or conical diffusers. Modified from: [24] . . . 27
2.13. 4 Types of honey combs. Source: [Author] . . . 28
2.14. Velocity profile throughout a wind tunnel. Source: [4] . . . 30
3.15. Wind tunnel CAD geometry. Source: [Author] . . . 31
3.16. Construction equipments. Source: [Author] . . . 32
3.17. Frontal and rear views of the wind tunnel fan. Source[Author] . . . 35
3.18. Test section: (a) test section built and (b) Detail A. Source:[Author] . . . 36
3.19. Honeycomb photo and (b) Detail B. Source: [Author]. . . . 38
3.20. Contractor dimensions. Source: [Author] . . . 39
3.21. Diffuser details: (a) Diffuser dimensions and (b) Pressure tap fittings. Source: [Author]. 41
3.22. Fan-diffuser transition. Source: [Author] . . . 43
3.23. Real velocity control. Source: [Author] . . . 44
3.24. Structure for supporting the wind tunnel sections. Source [Author] . . . 45
3.25. Structure details. Source: [Author] . . . 46
3.26. Disassembled wind tunnel. Source: [Author] . . . 47
3.27. Real Wind Tunnel. Source: [Author] . . . 48
4.28. Working mesh. Source: [Author] . . . 52
4.29. Y+ wall Contour at 20 m/s. Source: [Author] . . . 56
5.30. Pitot static tube. Source: [Author] . . . 58
5.31. Experimental measurements setup. Source: [Author] . . . 59
5.32. Experimental Setup. Source: [Author] . . . 60
5.33. Differential pressure measurements procedure. Source: [Author] . . . 61
5.34. Velocity plane in the center of the test section. Source: [Author] . . . 62
5.35. Experimental turbulence intensity at 20 m/s in the test section. Source[Author] . . 64
5.36. Test section mid plane in simulation: [Author] . . . 66

5.37. Simulation data recompilation. Source: [Author] 66
5.38. Velocity plane in the center of the test section based on simulation. Source: [Author] 67
5.39. Pressure along symmetry axis. Source: [Author] 68
5.40. Velocities planes comparation at 5 m/s. Source: [Author] 70
5.41. Velocities planes comparation at 10 m/s. Source: [Author] 71
5.42. Velocities planes comparation at 15 m/s. Source: [Author] 71
5.43. Velocities planes comparation at 20 m/S. Source: [Author] 72

Tables Index

3.1. Wind Tunnel Materials, Components, and Specifications 34
3.2. Pressure losses in wind tunnel 43
4.3. Simulation Parameters for Different Velocities 51
4.4. Mesh Independency with RMSE values. 52
4.5. Mesh Quality Parameters 52
4.6. Boundary Conditions and Model Parameters 55
4.7. Mean and Maximum y^+ values at different velocities in the test section 57
5.8. RPM Values for Different Desired Velocities 60
5.9. Sample Data of Experimental Differential Pressure at Point 12x12 62
5.10. Maximum and Average Percentage Errors for Each Experimental Velocity 63
5.11. Experimental Turbulence Intensity Values for Different Speeds 64
5.12. Pressure losses in wind tunnel 65
5.13. Maximum and Average Percentage Errors for Each Simulated Velocity 67
5.14. Pressure Along Symmetry Axis Collected 68
5.15. Experimental and simulated velocity values for different velocities. 72
5.16. Absolute error and percentage error values for different velocities. 73

Copyright

The author assures that the content of this project is their own work and does not constitute total or partial plagiarism of other works.



Author: _____
Alejandro Patiño Molano

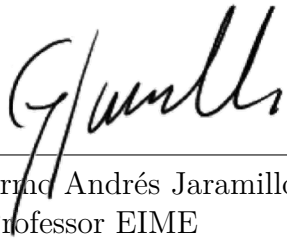

Director: _____
Eng. Guillermo Andrés Jaramillo Pizarro
Assistant Professor EIME



Copyright © Universidad del Valle

1. Introduction

In this chapter, a description of the concept and function of a wind tunnel is carried out, as well as a contextualization at a global and national level. The approach of the problem that is addressed in this work has been presented stressing its relevance to solve existing problems in the mechanical engineering school of the Universidad del Valle, followed by the background of the project, highlighting the achievements and scope obtained through the implementation of wind tunnels in various areas of knowledge. Subsequently, the presentation of the importance of carrying out this project is justified and endorsed with the methodology to accomplish the objectives proposed.

1.1. Contextual framework

The wind tunnels are instruments used to simulate airflow conditions around objects such as turbines, air vehicles, ground vehicles, or physical models to perform aerodynamic evaluations on these. They are an accurate option to develop reliable aerodynamic studies evaluating the behavior of the fluid flow around an object by means of trace lines, pressure measurements, drag or lift estimations using transducers or aerodynamic balances, etc [1]. The reliability of the information obtained from any wind tunnel is achieved with noise reduction, when there is a control on the boundary layer growth and obtaining low turbulence intensities. However, nowadays a great variety of these studies can be simulated with Computational Fluid Dynamics (CFD) accurately. Particularly, worldwide aeronautic agencies like NASA, have a broad selection of wind tunnels which are used to improve air transportation testing new ideas to build more effective and safer rockets or planes before its full scale manufacture [2]. In the automotive industry, wind tunnels seek to improve the aerodynamic performance of vehicles [3] and they are also used to evaluate aerodynamic effects in civil engineering infrastructure.

There are different classifications of wind tunnels based on their purpose, type of circuit or and, velocity range. Some of them, based on their purpose are used for aerodynamic evaluation on planes and land vehicles, shock waves dissipation, wind turbines performance, boundary layer separation, just to mention few of them. Based on their circuit, they are separated in closed-circuit wind tunnels that form a closed loop where the air is recirculated and open-circuit wind tunnels where the air is drawn in from the surroundings and discharged outside after passing through the equipment. Also they are organized based on their velocity range: Subsonic, for velocity magnitudes below the speed of sound with a Mach number (Ma) lower than 1; supersonic, for $1<Ma<5$ and hypersonic for $Ma>5$[4]. There are also other types of wind tunnels, among them there is the boundary layer wind tunnel that simulates a thin layer of air near the surface of an object just like the one that can be find in the civil engineering school at Universidad del Valle[5].

It is important to have this type of tools in an educational environment, as they validate airflow behaviors proposed theoretically or through simulation and lead students to understand

the physical behavior of the airflow in a controlled environment, providing them with a deeper understanding of the physical meaning beyond what a simulation can offer. This does not mean diminishing the importance of simulation but rather complementing it, like determining experimentally the efficiency on a new proposal of wind microturbines, a real project carried out on a wind tunnel model built by the team Vortex inside the research team IMPETUS INDOMITUS [6], where, thanks to this tool, it was possible to compare the actual behavior of a microturbine proposal.

1.2. Problem statement

Universidad del Valle is recognized for the quality in the training of its students. In 2005, the university obtained the high-quality institutional accreditation, which was renewed in 2014 for ten more years [7] and in 2024 was renewed for another 10 years. In the area of thermo-fluids of the school of mechanical engineering there are currently several projects that are carried out such as the development of aerodynamic balances, identification of aerodynamic performance of wing profiles by means of simulation with CFD using OpenFoam and ANSYS Fluent (student license), programs through which efficient data can be obtained but these must be contrasted with experimental data to be validated. The mechanical engineering school has equipment to make experimental measurements such as a water tunnel and a fan characterization duct. In addition, it has the necessary tools to develop fluid machinery such as water pumps and axial or centrifugal fans from 3-D printing. The manufacturing of these machines is an important part of the Fluid Machines course (780065M). However, despite the fact that there are currently graduate works detailing the construction and implementation of different types of wind tunnels and elements for these [8] [9] [10]. So far, there is not any multipurpose wind tunnel with all the necessary adaptations for such operation in this school. Despite the fact that the Universidad del Valle has two wind tunnels, one for the school of civil engineering and the other for the school of architecture, these wind tunnels are not suitable for aerodynamic evaluations since they are designed to have a detachment of boundary layer and it can not be controlled.

The School of Mechanical Engineering currently funds multiple projects and expenses, including the conversion of a vehicle to electric operation [11], which also receives support from SENA. Consequently, there is limited funding available for the development of a large-scale wind tunnel, such as the one at the Civil Engineering School [5]. If there is a need for this equipment, a cost-effective and compact solution may be preferable, such as subsonic wind tunnels with low energy consumption and with smaller space requirements, like open-circuit wind tunnels. Additionally, a modular design would facilitate transportation and the interchangeability of its sections to evaluate various phenomena. Given these considerations and the velocity profile inside the test section of a wind tunnel has to be as constant as possible, the following question arises: What is the velocity profile experimentally recorded in the test section of an open-circuit modular subsonic wind tunnel built at the Universidad del Valle for velocities up to 20 m/s?

1.3. Problem tree

Due to the issue depicted earlier, figure 1.1 presents the problem tree for this project. It highlights the core problem at the center and the primary potential causes located in the lower section of the figure. The current consequences of this problem are shown in the upper section.

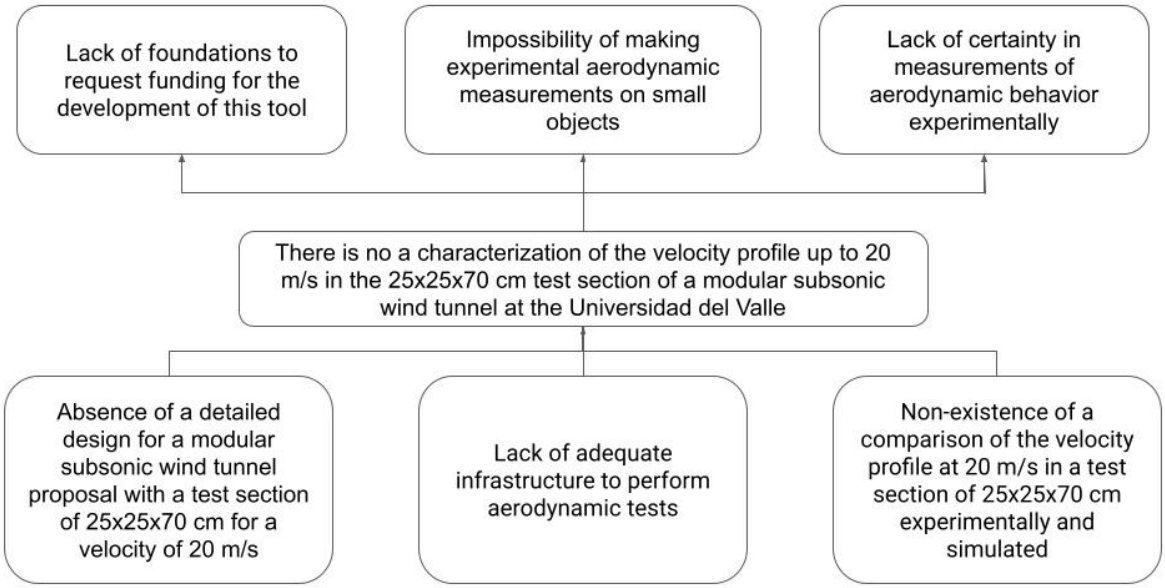

Figure 1.1: Problem tree diagram. Source: [Author]

1.4. Literature review

In this section, the origins of wind tunnels and their evolution up to the present day are showcased. The various types that exist now are described, and the first wind tunnel built in Colombia is highlighted for its historical significance.

1.4.1. History

For the various advances in aerodynamics and fluid mechanics, wind tunnels have been a great ally in the investigation of aerodynamic profiles, resistance and drag evaluation, studies of aerodynamic phenomena and the validation of complex numerical models. These advancements have played a fundamental role in shaping the contemporary world. Their outcomes are evident in the modernization of commercial, cargo, and military aircrafts, as well as in the automotive industry, wind energy, and the burgeoning field of Unmanned Aerial Vehicles (UAVs). These UAVs find applications in various sectors including agriculture, surveying, civil engineering, the film industry, and more [12]. For the various advances in these areas of knowledge, wind tunnels have played a very important role, since they allow the simulation of flow conditions in a controlled environment, which facilitates the evaluation of aerodynamic effects on elements subjected to tests.

The origin of these aerodynamic evaluation tools dates back to the year 1871 in Greenwich, England. It was designed and built by marine engineer Francis Wenham and firearms designer John Browning. This first tunnel was only 3 ft long and had a test section with an 18 in edge length. The lift and drag force of a model located at the end of the wind tunnel were measured. These forces were produced by a forced draft axial fan (which pushed the air towards the wind tunnel) and were measured by determining the weight of the bars attached to the model [13]. This first wind tunnel was born from Wenham's need to determine the aerodynamic behavior of

a proposal for superimposed wings for a model airplane, since in 1858 he built a glider with up to five stacked wings. but it was not successful. However, in 1866 he patented this design, which became pillar for model airplanes that became popular at the end of the 19th century. This model was based on extending the aerodynamic area of the wings to reduce their length and generate better lift. Having reduced the length of the wings, structural problems were avoided at the time of construction.

Years later, in 1901, the Wright brothers used a wind tunnel to study the aerodynamic effects on different wing profiles for the construction of their model aircraft, which was successful despite the inadequate operation of their wind tunnel (see figure1.2). The parameters of the Wright brothers' wind tunnel model were not rigorous because they did not have much knowledge in fluid mechanics, which is why their design was discarded despite successful results in the tests of their airfoils [12].

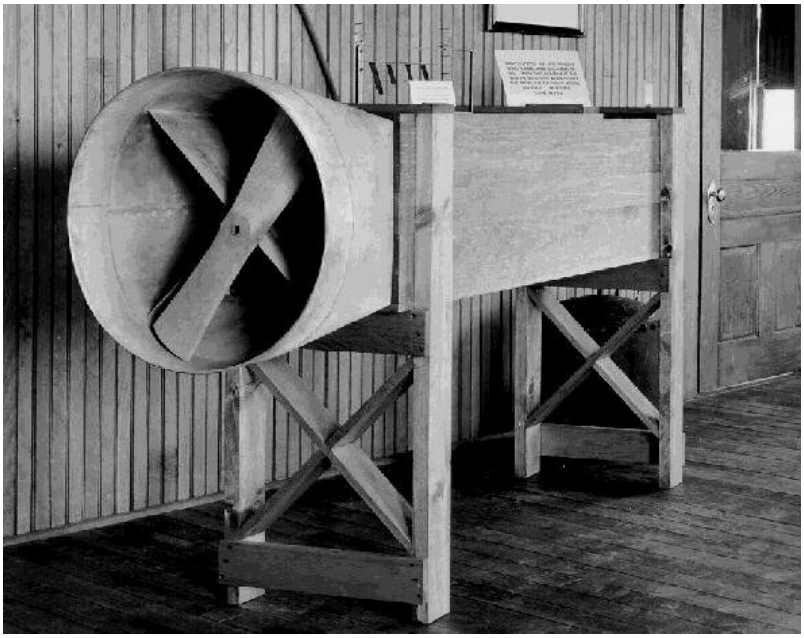

Figure 1.2: Wright brothers wind tunnel replica made in 1938. Source: [12]

As the use of aircraft became more frequent, the requirement for larger wind tunnels became essential for their advancement and improvement. For this reason, better and larger facilities were created each time, where the full-scale models could be tested before carrying out their first test flight. Years later, thanks to the growth of the aerospace and automotive industries, the functions of wind tunnels also diversified. In the United States, for instance, in 1955 the National Aeronautics and Space Agency (NASA) finished the construction of the Unitary Plan Wind Tunnel at NASA's Ames Research Center in California. which is a facility that included transonic and supersonic test sections, enabling detailed studies of flow compressibility and shock waves with the intention of implementing their findings in aircraft development. For this, the wind tunnels reach Mach numbers between 0.8 and 1.2 to enter into a transonic range [14].

Wind tunnels come in different sizes and serve various purposes. Generally, small wind tunnels are used for academic research. In these, professors and students can visualize aerodynamic phenomena or test new developments, as the objects placed in the test section can be scaled. Designing and building a wind tunnel also presents a valuable challenge for students at different universities. This has been the case in many universities worldwide, such as the University of Emden-Leer, Leinz, and Münster, to name a few, whose wind tunnels can be appreciated in Figure 1.3

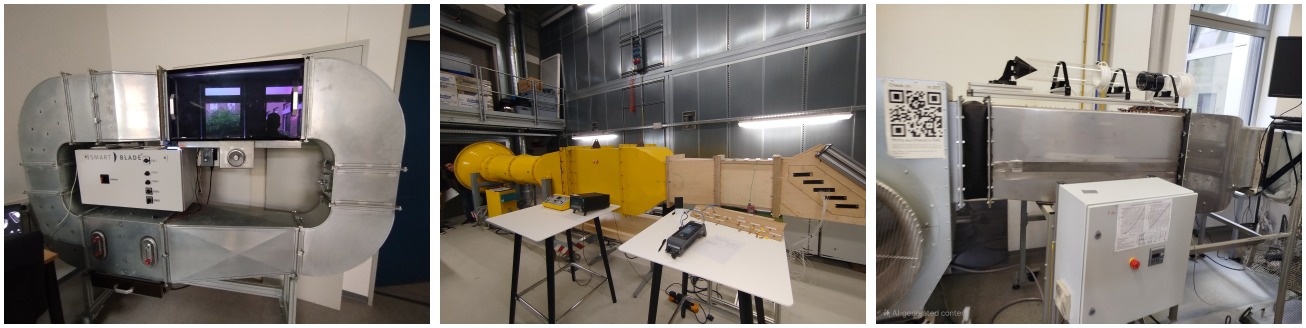

(a) Wind tunnel at University of Emden-Leer **(b)** Wind tunnel at University of Leinz **(c)** Wind tunnel at University of Münster

Figure 1.3: Small-scale academic wind tunnels used for research and educational purposes in different universities. Source [Author]

1.4.2. Wind tunnels in Colombia

In Colombia there are also several institutions that have wind tunnels, some of them have been manufactured by the same institutions. Among the first to design and build a wind tunnel in Colombia is the Universidad Nacional de Colombia. Therefore it must be highlighted this is not a work being addressed for the first time. However, their construction and manufacturing are. Similar works have already been carried out in different institutions around the world[15] and even in Colombia where one of the first record of construction of a open circuit wind tunnel took place at the Universidad Nacional de Colombia in 2011[16]. Roberto Martínez, professor of the Department of Physics of this university was the designer of this subsonic wind tunnel seen in figure 1.4 that had a low cost of 6 million pesos and is currently used by the departments of mechanical, agricultural, civil and architecture engineering to carry out different studies. This same intention that is had in this project, to create development to favor the student community .

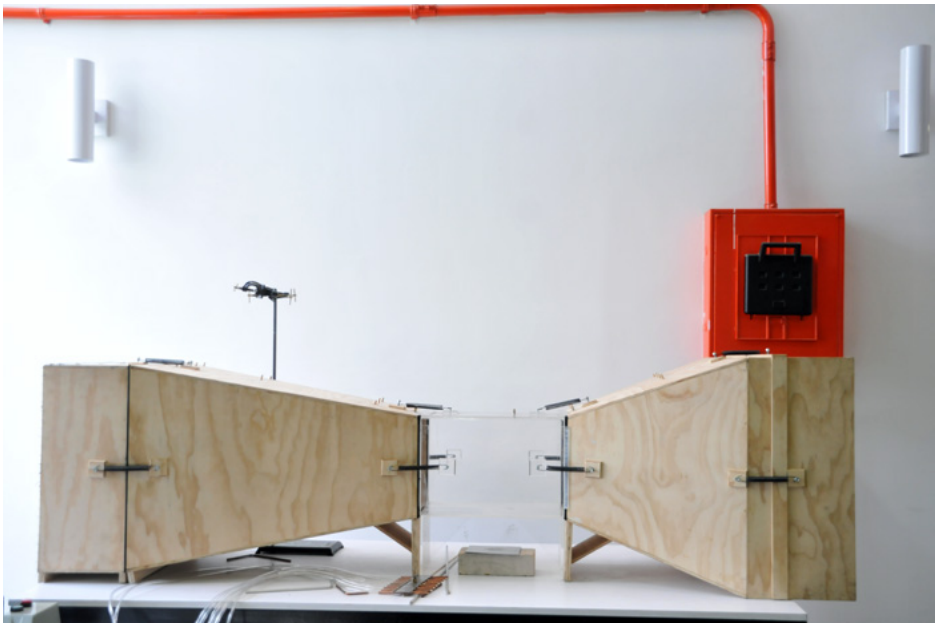

Figure 1.4: First wind tunnel in Colombia. Source:[16]

Previously. in 2008 the Universidad de los Andes in Bogotá, Colombia submitted a Master's thesis where Santiago Caicedo, its author, explained the procedure he used to build a closed circuit wind tunnel for aerodynamic tests up to 60 m/s and test section dimensions of 1mx1mx2m. The wind tunnel was called TVIM-49-60-1X1 and it is used for academic purposes to show the students the different physical phenomena and the different topics in fluids dynamics [17].

At the Universidad del Valle, the School of Civil Engineering acquired a wind tunnel , a few years ago, which is used for experimental evaluation of wind effects on structures, atmospheric pollutant dispersion, pedestrian comfort in urban spaces, and other applications [5]. The School of Mechanical Engineering in 2024 now houses its own wind tunnel, designed and constructed by the research team Impetus Indomitus. This equipment has already played a pivotal role in supporting four undergraduate theses and one master thesis, showcasing its value as a crucial asset for hands-on learning and research. Its availability underscores a growing academic interest in experimental aerodynamics and applied fluid mechanics, providing students and researchers with the opportunity to explore complex aerodynamic phenomena and validate computational models in a controlled environment. This tool not only enhances the academic and practical capabilities of the department but also opens new pathways for innovative research and collaboration in the field of mechanical engineering.

1.4.3. State of the art

Nowadays, NASA has tunnels in lengths of a few inches, which are used to test the aerodynamic behavior of scale parts of airplane models, and also has wind tunnels so large that they can even evaluate full-scale aircraft. Of all the space agencies in the world, NASA has the largest and most modern wind tunnel, called the Flight Research Unit (FRW) wind tunnel, located at the NASA Langley Research Center in Virginia. This tunnel, with a length of more than 36 meters, has the capacity to carry out aerodynamic tests on large-scale aircraft models. They also have wind tunnels for testing at hypersonic speeds of up to 6,400 km/h [2].

The German Aerospace Center (DLR) also operates advanced wind tunnels, including the Cologne Cryogenic Wind Tunnel, which allows for testing at variable pressures and temperatures, making it a crucial tool for aerospace and high-speed train development. Similarly, the China National Space Administration (CNSA) has established state-of-the-art hypersonic wind tunnels, like the JF-12 tunnel in Beijing, capable of simulating speeds up to Mach 9, which are pivotal for developing spacecraft and hypersonic vehicles. The Russian space agency (Roscosmos) continues to utilize and upgrade the Central Aerohydrodynamic Institute (TsAGI) wind tunnel facilities, which have historically been essential in the development of both Soviet and modern Russian aerospace technologies. Together, these agencies maintain robust wind tunnel programs that complement and, in some cases, rival NASA's capabilities, contributing to the global advancement of aerospace research and technology.

Despite significant advances in the construction and operation of wind tunnels, there are persistent challenges. For example, the homogeneity and stability of the flow, the precision of measurements and the minimization of interferences are key aspects to ensure the reliability and precision of the results obtained in a wind tunnel. Therefore, it is crucial to thoroughly investigate and understand the theoretical and practical aspects related to the construction and operation of wind tunnels.

The advances that have been made in this era have allowed the new wind tunnels to not only circulate air as a fluid, but also to transport other types of substances, such as the case of one of the tunnels of wind of the European Space Agency (ESA), which is designed to transport plasma

as seen in the figure 1.5, which is an ionized gas. This type of wind tunnel is used to generate more realistic flight conditions since it reaches high temperatures and also velocities greater than those of gases [18]. This image shows a plasma wind tunnel test, where a model, where a CubeSat is exposed to extreme conditions simulating atmospheric reentry. The test includes top and side views, illustrating how the plasma interacts with the model, with intense colors highlighting areas of high heat emission. These experiments are crucial for understanding how materials and structures withstand the intense heat and aerodynamic forces experienced during reentry, helping to develop advanced thermal protection technologies.

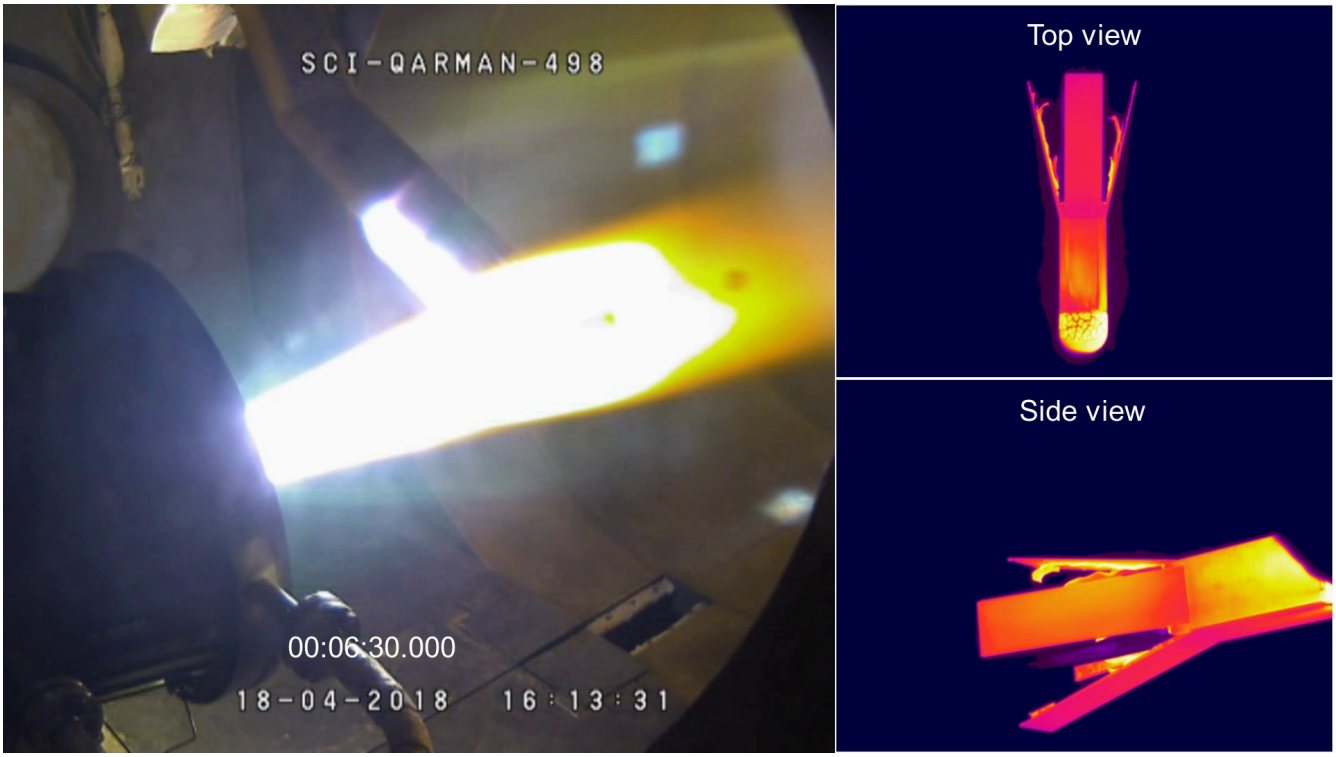

Figure 1.5: Plasma wind tunnel testing. Source: [18]

In addition to these, around the world various institutions have different types of wind tunnels that can be found in the reference [19], where there is a real-time map where can be seen the main facilities where that posses wind tunnels. However, not all of them are found since in Colombia no location is listed despite the fact that there are different institutions that have registered wind tunnels.

Wind tunnels have evolved with the advancement of technology and computing. Subsonic, supersonic, and hypersonic wind tunnels have been developed to address a wide range of applications. In addition, numerical simulation techniques and CFD modeling have been implemented to complement the experimental data obtained in wind tunnels. On the other hand, they are used for a wide variety of purposes such as urbanization, testing of new technologies and more. Among the programs in which CFD simulations can be carried out are Comsol, ANSYS Fluent, OpenFoam, Star-CCM+, Autodesk and SimScale. These programs over time have come to present results so precise that experimental tests are no longer necessary and the simulation results are trusted. This technological advance has led many wind tunnel facilities in the United States to close since their use requires much more energy than the required for a computer to carry out a simulation [20].

1.5. Justification

The experimental method allows to obtain information that simulation does not, testing hypotheses, validating theories, and obtaining quantitative results that support or refute theoretical predictions [21]. While equations and simulations are powerful tools for modeling and predicting the behavior of physical phenomena, experimental tests provide direct validation and verification of proposed theories and models. Through experimental tests, it is possible to obtain empirical data and real observations that allow to evaluate the accuracy of theoretical models, identify possible discrepancies, and discover new aspects that could have been overlooked. In addition, experimental tests provide an opportunity to study complex and nonlinear phenomena that are difficult to describe with equations alone [22]. One of the strengths of the experimental method is its characteristic to control specific variables and conditions, which makes it possible to isolate the relevant factors and analyze their influence on the phenomenon studied. In addition, it allows the detection of causal relationships, the identification of patterns and the generation of new knowledge.

The lack of a precise characterization of the velocity profile up to 20 m/s in the 20x20x70cm test section of a wind tunnel limited the understanding of the airflow behavior and could have affected the accuracy and reliability of the results obtained in aerodynamic tests. This could have lead to misinterpretation of aerodynamic phenomena and make it difficult to design and optimize objects and models undergoing wind tunnel tests. Therefore, was essential to carry out an exhaustive study that allows to accurately characterize the velocity profile in the test section of the open-circuit modular subsonic wind tunnel. This characterization with detailed measurements at different points and operating conditions, with the aim of better understanding flow patterns and their influence on aerodynamic tests.

The wind tunnel was entirely constructed by the author of this thesis, an undergraduate student, using polylactic acid (PLA) via a 3D printer and polymethyl methacrylate (PMMA). This aspect makes it a tool that can be easily reproduced using its blueprints provided by accessing to the following link: "https://drive.google.com/drive/u/0/folders/1g2qaZ40NcKeajxSLQDBS3GWtTMKWy5ze". The motivation behind this project is providing a structure, low cost equipment and corroboration of proper functioning of a wind tunnel so that it can be freely used by any student at Universidad del Valle. The reason to implement a modular structure was to have the possibility of transferring the equipment from one place to another. In addition, the modular type and the materials were selected to have interchangeable test sections and to be low cost since the wind tunnels that are in the market with similar dimensions are around the values of $ 20.322 USD [23].

1.6. Objectives

In this section, the text displays the general objective that will guide the progression of this project, as well as the specific objectives developed to attain it.

1.6.1. General objective

Characterize the velocity profile in the test section of a modular open circuit subsonic wind tunnel with a range of velocities up to 20 m/s at the Universidad del Valle.

1.6.2. Specific objectives

1. Design in detail a proposal for a modular open circuit subsonic wind tunnel with a test section of cross sectional area of 25x25x70 cm at velocities up to 20 m/s.

2. Build the wind tunnel of the proposal obtained.

3. Compare the velocity profile obtained experimentally in the test section of the wind tunnel with analytical or simulation results.

1.6.3. Objectives tree

As a result of the problem tree analysis, a solution to the identified problem is defined. Figure 1.6 illustrates the objectives tree diagram, with the general objective of this work at the center. Below are the specific objectives designed to achieve the general objective, and at the top are the expected outcomes resulting from the implementation of each objective.

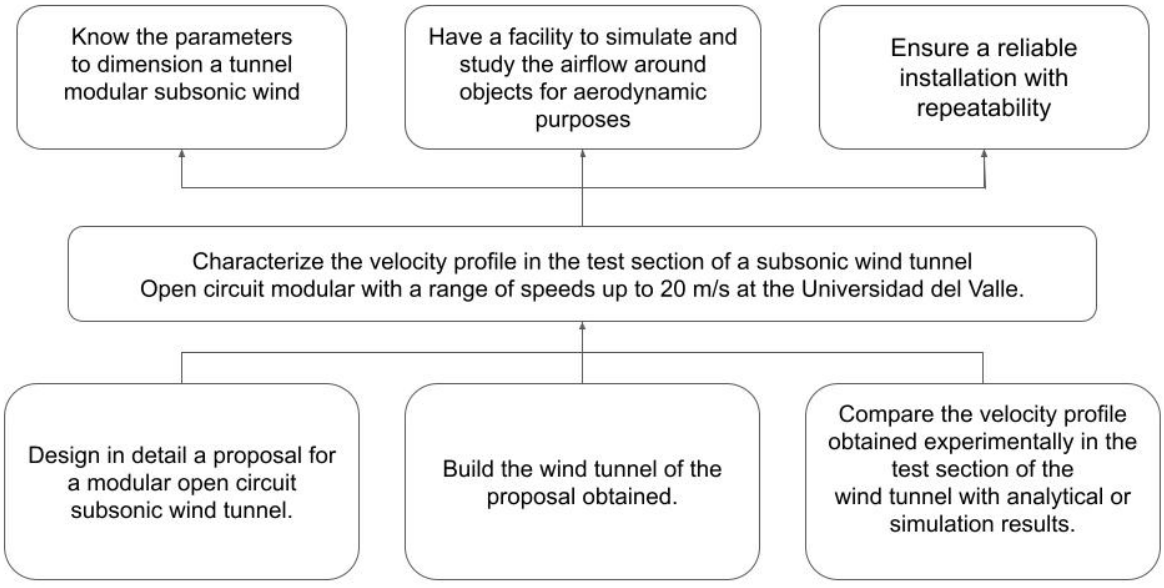

Figure 1.6: Objectives tree diagram. Source: [Author]

1.7. Methodology

A series of activities, outlined in Figure 1.7, were carefully planned and organized to fulfill each of the three specific objectives. This structured approach not only ensures that each objective is systematically addressed but also facilitates efficient project time management. By breaking down the project into detailed, manageable tasks, the progress can be tracked effectively.

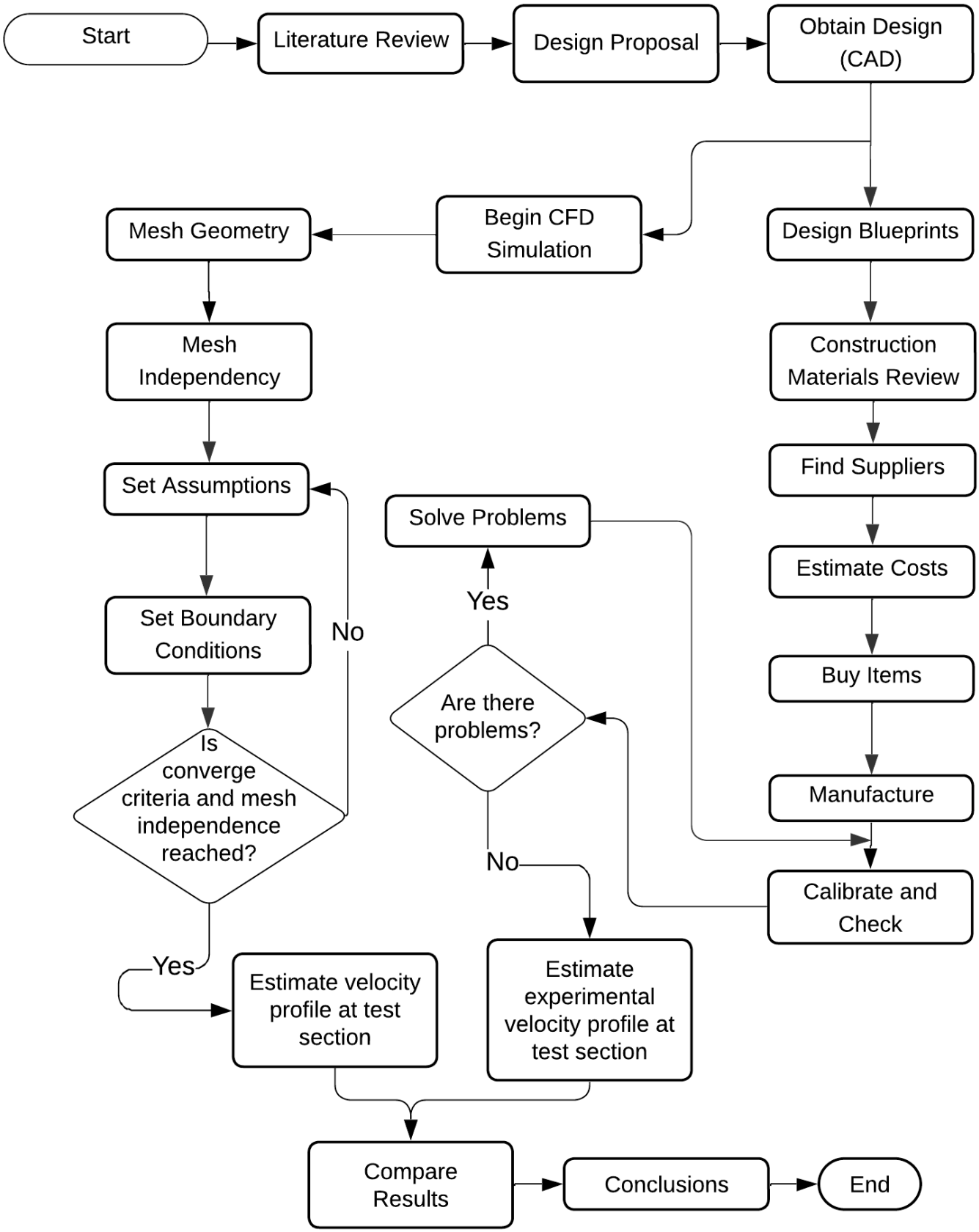

Figure 1.7: Project flow diagram. Source: [Author]

To address the objectives of this project, an experimental setup will be conducted to measure velocity at various points across the mid-plane of the wind tunnel test section. The process begins with a thorough literature review and analysis of the state-of-the-art on wind tunnels, which includes studying previous research to identify if similar projects have already been completed. Understanding these existing designs will provide a foundation for introducing innovative improvements, whether by optimizing current designs or incorporating new features to enhance performance and functionality. The goal is to pinpoint areas where the project offers novel contributions. Upon completing the literature review, the next phase involves the detailed design of all components of the wind tunnel. This design must specify dimensions, materials, and methods for assembling the parts, which could include welding, couplings, flanges, or screws. Once the design details are outlined, Computer-Aided Design (CAD) models of the geometries will be created, enabling fluid simulations to verify if the proposed design will deliver a straight and uniform velocity profile within the test section.

The next step is to generate the mesh for the simulation, ensuring that smaller elements are used near the boundaries to accurately represent the physical phenomena and that thehat the mesh independeconducted.nducted.

For the simulations, understanding the underlying physics of the phenomenon is essential for making appropriate assumptions and setting accurate boundary conditions. Since simulations will be conducted using OpenFOAM (Open-source Field Operation and Manipulation), the setup should accurately reflect actual conditions. Once the simulations are completed, the collected velocity data must be saved for later comparison against the experimental results.

After confirming the design through simulations, construction of the wind tunnel can proceed according to the specifications established. This phase is expected to be time-intensive because it involves processes such as welding and 3D printing, which can take over 24 hours for each component. However, while the components are being printed, the methodology for measuring the velocities is established.

Sourcing materials is another crucial aspect. Possible material sources include the mechanical engineering department, research teams, personal resources, or existing supplies from the fluid mechanics laboratory. Based on the design and specified dimensions, suitable materials are selected. For this project, materials include PLA (Polylactic Acid) for 3D-printed components, acrylic for the test section to ensure visibility, and steel for the structure, chosen for its strength to support the weight of the tunnel sections.

The construction starts by 3D printing the components that can be printed while simultaneously working on other tasks, such as preparing the frame. The budget was created, considering that some prices might vary or that more investment might be needed in certain areas. Thanks to this, the planned funds were sufficient for the construction expenses. However, since part of the construction funds were provided by the school, the discounts for stamps and the withholding tax were not taken into account, so part of the budget was covered by the research team and the student.

After construction is completed, experimental measurements of the velocity profile will be carried out. These measurements will be statistically analyzed by collecting multiple data points at each location to determine the reproducibility of the wind tunnel and verify uniformity across the cross-section. Measurements will be taken at intervals of 5 m/s, ranging from 5 to 20 m/s, with the aid of a frequency inverter connected to the motor. A sampling frequency will be established to gather data. The points for velocity measurements will match those from the simulation, ensuring a comprehensive experimental setup.

Finally, the data gathered from simulations will be compared to experimental results. Ad-

ditionally, uncertainty analysis will be conducted to validate the reliability of the experimental methodology.

1.8. Expected impact

It is expected to make an impact on the University of Valle's community by providing a tool through which various fluid phenomena and topics, previously only approached analytically or through simulation at the university, can be explored. This wind tunnel is anticipated to serve as the foundation for many undergraduate and postgraduate students to develop thesis proposals, fostering their research skills and practical knowledge in the field of fluid dynamics. Furthermore, it is envisioned that this facility will encourage interdisciplinary collaboration and innovation, opening up opportunities for faculty and students to undertake cutting-edge research projects and advance our understanding of fluid dynamics

2. Theoretical framework

This chapter provides an in-depth exploration of fundamental aspects related to wind tunnels, encompassing their classification, primary components, and essential concepts. It delves into the physical parameters crucial for understanding airflow behavior, accompanied by the key equations that validate these parameters within the context of wind tunnel operation. Additionally, it discusses the pressure distribution inside these testing tools and explains the expected velocity profile in the test section, along with the underlying principles driving this behavior. By covering these elements, the chapter establishes a theoretical foundation necessary for both the development and understanding of the project, ensuring a comprehensive grasp of the factors influencing wind tunnel performance and experimental accuracy.

2.1. Open circuit wind tunnel

These open circuit wind tunnels operate by drawing in atmospheric air and expelling it back into the atmosphere, in contrast to closed circuit wind tunnels that recirculate air for reuse. A fan propels the air into the wind tunnel, and this configuration can be situated either at the tunnel entrance or its exit, resulting in two distinct types of open circuit wind tunnels [24].

In an induced draft wind tunnel, the fan is positioned at the tunnel exit, creating a zone of low pressure that draws air in from the entrance. This method provides a controlled and steady airflow throughout the tunnel. The object being tested is placed within the test section, exposed to the controlled airflow, and the corresponding data is recorded. Conversely, in a forced draft wind tunnel, the fan is situated at the tunnel entrance, pushing air towards the exit. This approach is employed when higher velocities and a constant pressure airflow are required. Both of these wind tunnel types are illustrated in Figure 2.8.

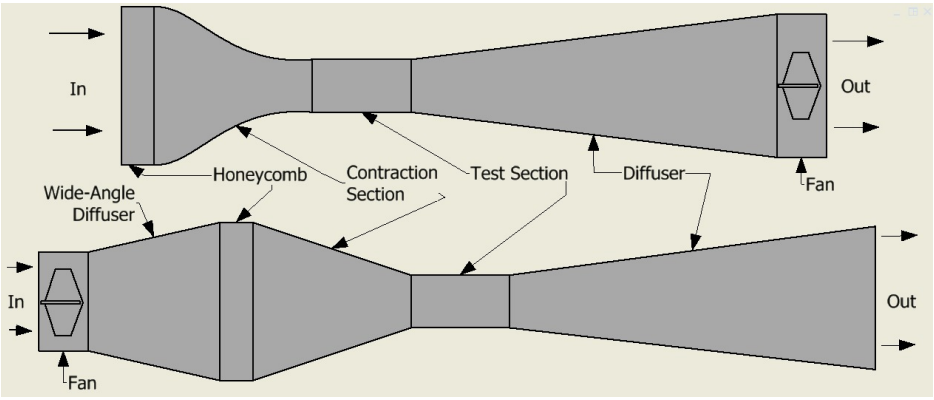

Figure 2.8: Suck-down (top) wind tunnel and Blow-down (down) wind tunnel. Source:[Author]

Open circuit wind tunnels offer several advantages over closed circuit wind tunnels. They are cost-effective to manufacture as they do not require flow redirection components. Additionally, these wind tunnels provide the flexibility of releasing smoke into the atmosphere for visual evaluation of phenomena. However, open circuit wind tunnels have their drawbacks. Notably, they require an efficient flow direction system at the tunnel entrance since air enters the contraction zone from all directions. Therefore, a flow straightening system, known as a honeycomb, is essential prior to the contraction zone, and screens are employed to direct the flow.

The primary components of a wind tunnel are the contraction,the test section, and the diffuser. The effective operation of the wind tunnel hinges on the well-thought-out design of these three fundamental sections. Additionally, other components include screens, a honeycomb, and the fan structure, all of which contribute to the performance of the wind tunnel. Each section must meet specific design conditions to ensure that flow detachment is prevented.

When operating with subsonic speeds and considering air as the working fluid within a wind tunnel, it can be assumed that the fluid is incompressible if Ma<0.3. In this context, 'incompressible' means that the density of the air remains constant throughout the entire process. Another key assumption in wind tunnel operation is that the incoming mass flow rate is equal to the outgoing mass flow rate, and no mass remains within the control volume delimited by these sections. This is due to the fact that there is only one entrance, located within the contraction zone, and one exit, which is positioned after the diffuser. Thus, starting with the initial equation in 2.1, which represents the differential form of the continuity equation for a compressible flow, we can, by assuming incompressibility and a steady-state condition, derive the final equation for conservation of flow rate. This equation is essential for the design of wind tunnels as it allows for the calculation of losses and determination of the required flow rate.

$$
\begin{aligned}
&\frac{\partial \rho}{\partial t} + \frac{\partial(\rho v_x)}{\partial x} + \frac{\partial(\rho v_y)}{\partial y} + \frac{\partial(\rho v_z)}{\partial z} = 0 \\
&\int_{CV} \left(\frac{\partial \rho}{\partial t} + \nabla \cdot (\rho \mathbf{v}) \right) dV = 0 \\
&\int_{CV} \frac{\partial \rho}{\partial t}\, dV + \int_{CV} \nabla \cdot (\rho \mathbf{v})\, dV = 0 \\
&\int_{CV} \frac{\partial \rho}{\partial t}\, dV + \oint_{CS} \rho \mathbf{v} \cdot d\mathbf{A} = 0 \\
&\frac{\partial}{\partial t} \int_{CV} \rho\, dV + \oint_{CS} \rho \mathbf{v} \cdot d\mathbf{A} = 0 \\
&\rho \oint_{CS} \mathbf{v} \cdot d\mathbf{A} = 0 \\
&\oint_{CS} \mathbf{v} \cdot d\mathbf{A} = 0
\end{aligned}
\tag{2.1}
$$

2.2. Open circuit wind tunnel sections

This section focuses on the design and construction parameters for the wind tunnel components, aimed to set a uniform velocity profile within the test section while minimizing pressure drop throughout the entire wind tunnel. This objective aligns with the purpose of these tools.

2.2.1. Contraction section

The contraction section increases the velocity of the fluid entering the wind tunnel while decreasing the pressure through, as its name suggests, a softened contraction directs the flow to the test section, reducing pressure losses and avoiding the detachment of boundary layer by having a polynomial curve. This section is shaped by a polynomial expression which after experimental test done by James Bell and Rabindra Mehta [25] for a subsonic wind tunnel, a suitable contraction is obtained by a 5th order polynomial as described in equation 2.2. For the flow to circulate smoothly, the best cross section that can be chosen for this area is a circular section because there is no recirculation of the flow and the entire section is constant. As the rectangular cross sections do not meet this characteristic, they have secondary flows caused in the area of intersection of the edges, however these flows do not affect the proper functioning of the wind tunnel.

$$y(x) = H_i - (H_i - H_e)[6(x')^5 - 15(x')^4 + 10(x')^3] \tag{2.2}$$

Where H_i refers to the inlet height, H_e refers to the outlet height (The height refers to the distance between the axisymmetric line and the surface of a side of the contraction section) and x' is the position x divided by the total contraction zone length. In figure 2.9 the 5th order polynomial is plotted where the flow occurs from the left side to the right side.

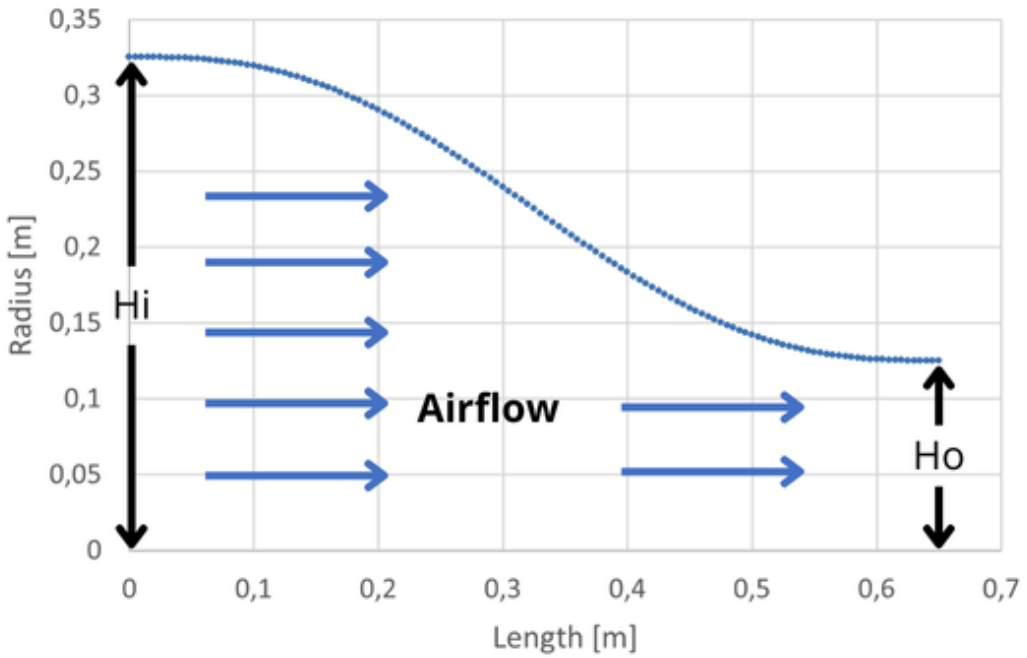

Figure 2.9: 5th Order polynomial contraction section side shape. Source: [Author]

It is important to parameterize precisely this design because a boundary layer separation may occurs when the contraction exceeds the relation length over inlet radius equals to 1.79 because a long contraction section length causes the boundary layer to thicken at the exit of its section [25]. Also if this section has that relationship lower than 0.89 there is also boundary layer separation but in its inlet. Another important design parameter for the construction is the area relation (AR) which is the outlet section area over the inlet section area. This relation must be between 0.100 and 0.167. The tests carried out for the optimization of subsonic wind tunnels performed by by Bell and Metha are valid for test sections with areas smaller than 0.5 m^2.

2.2.2. Test section

For these type of wind tunnels the most common test section is a rectangular cross-sectional shape with a hatch on one of its sides to introduce the models. For aeronautical purposes the length of this section is usually one or two times one of its sides dimensions but this can vary if the velocity profile is not uniform when reaches the object. The dimensions of this sections are among the first aspect to be determinate because the dimensions given will limit the objects to be tested. To avoid wall perturbations on the velocity profile the object to be evaluated has to be maximum 0.8 the edge length dimension as in shown in figure 2.10 where "d_{hts}" is the hydraulic diameter of the test section[1] And the airfoil length "$< 0{,}8 * d_{hts}$" indicates that it must not exceed that size. However, the maximum cross-sectional area that the object can occupy is 30 %, according to the American Institute of Aeronautics and Astronautics (AIAA)[26].

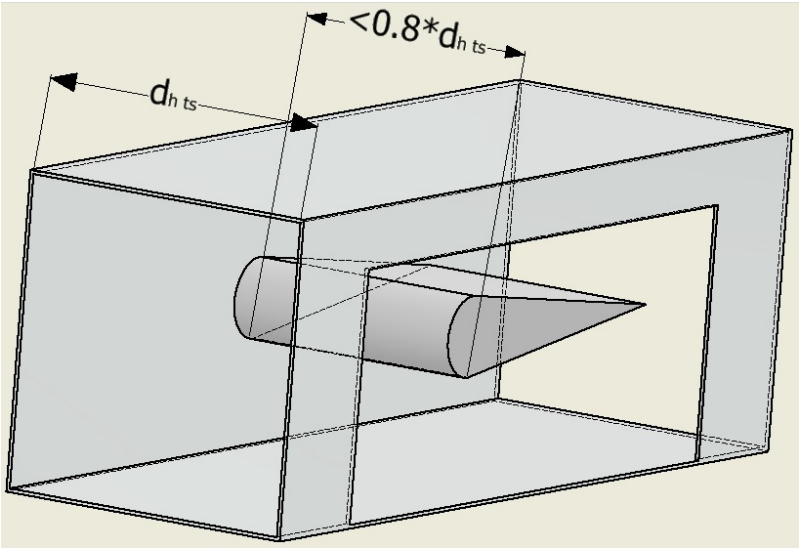

Figure 2.10: Test section length restriction Source: [Author]

2.2.3. Diffuser

This section is in charge of expanding the flow that comes from the test section. When this expansion occurs, the velocity of the fluid decreases but its static pressure increases. A progressive growth with an opening angle (θ) up to 3° is essential to avoid the generation of an adverse pressure gradient which would cause boundary layer separation [1]. As in the contraction section, a circular cross-sectional area avoids the presence of secondary flows, however if the cross-sectional area is not circular if the design parameters are respected, these flows does not grow much and do not generate recirculation. Although the performance is better in a conical diffuser for the same efficiency a conical diffuser is up to 8 times larger than a cross sectional [1]. In figure 2.11, three different types of diffusers views from one plane of symmetry are depicted. The first type features a circular inlet and outlet, the second type has a rectangular inlet and a rectangular outlet, and the last one has a rectangular inlet and a circular outlet. When the outlet is circular, there is no need to incorporate an additional section for fan adaptation.

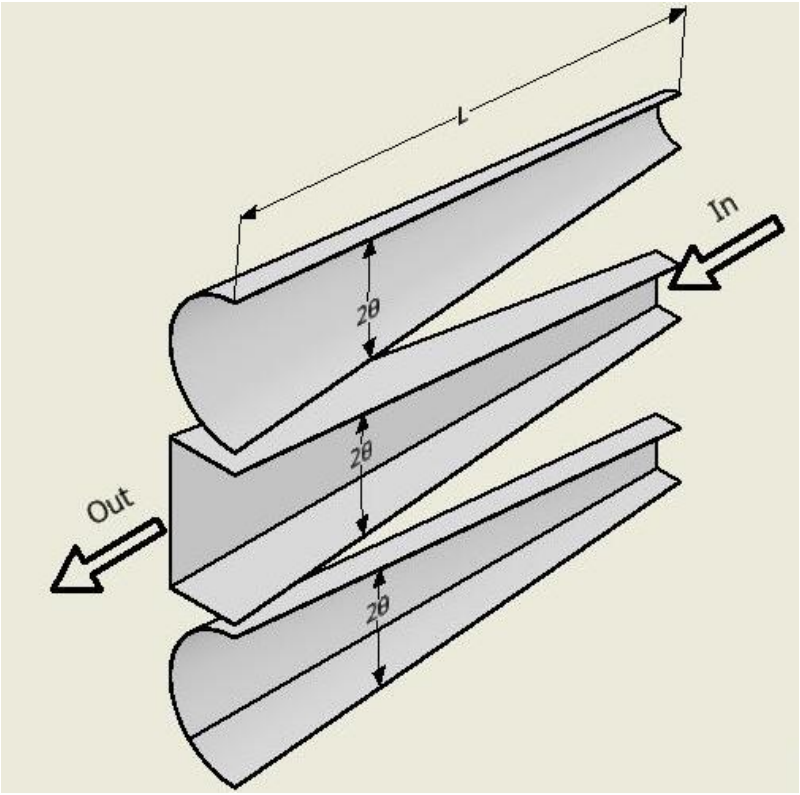

Figure 2.11: Three different diffuser geometries Source: [Author]

To parameterize the diffusers design, the Bernoulli equation (equation 2.3) was used where subindices in and out stand for inlet and outlet respectively. Assuming incompressible flow, no gravity effects and neglecting losses on the diffuser, equation 2.3 is reduced to equation 2.4 which is the equation for stagnation pressure (P_{Stg}), that is the pressure when the velocity is 0. The first term (P) is the static pressure, the dynamic pressure ($\frac{\rho v^2}{2}$) is the second term; and the head pressure ($\rho g h$) the third.

$$P_{in} + \frac{\rho v_{in}^2}{2} + \rho g h_{in} = P_{out} + \frac{\rho v_{out}^2}{2} + \rho g h_{out} \tag{2.3}$$

$$P + \frac{\rho v^2}{2} + = P_{Stg} \tag{2.4}$$

When delving into the intricacies of diffusers, it becomes imperative to thoroughly assess the pressure loss coefficient, denoted as c_p. This coefficient serves as a pivotal output measure, as its magnitude significantly influences the diffuser performance. A higher value of c_p is indicative of an enhanced diffuser efficiency. The precise definition of this coefficient can be found in equation 2.5, where its evaluation is crucial for a comprehensive understanding of the diffuser operational characteristics and overall effectiveness.

$$c_p = \frac{P_{in} - P_{out}}{P_{Stg} - P_1} \tag{2.5}$$

By employing the equation of mass conservation and integrating it with the principles outlined in 2.3 and 2.5, a comprehensive description of diffuser performance emerges. This intricate relationship is encapsulated by the ratio of areas, denoted as the Area Ratio (AR), expressed as

the quotient of the exit area (A_2) to the entrance area (A_1). The mathematical representation of this critical aspect is precisely elucidated in equation 2.6. This equation not only encapsulates the interplay between mass conservation, Bernoulli's equation, and the pressure loss coefficient but also serves as a fundamental expression that unveils the nuanced dynamics governing the diffuser operational efficacy in terms of its geometric characteristics.

$$c_p = 1 - AR^{-2} \tag{2.6}$$

With this parameter and the relation between length and radius at the exit, using the figure 2.12 the working dimension is defined. If the relation between these two magnitudes is between the colored region, up to the conical line if conical diffuser, then the diffuser will perform adequate.

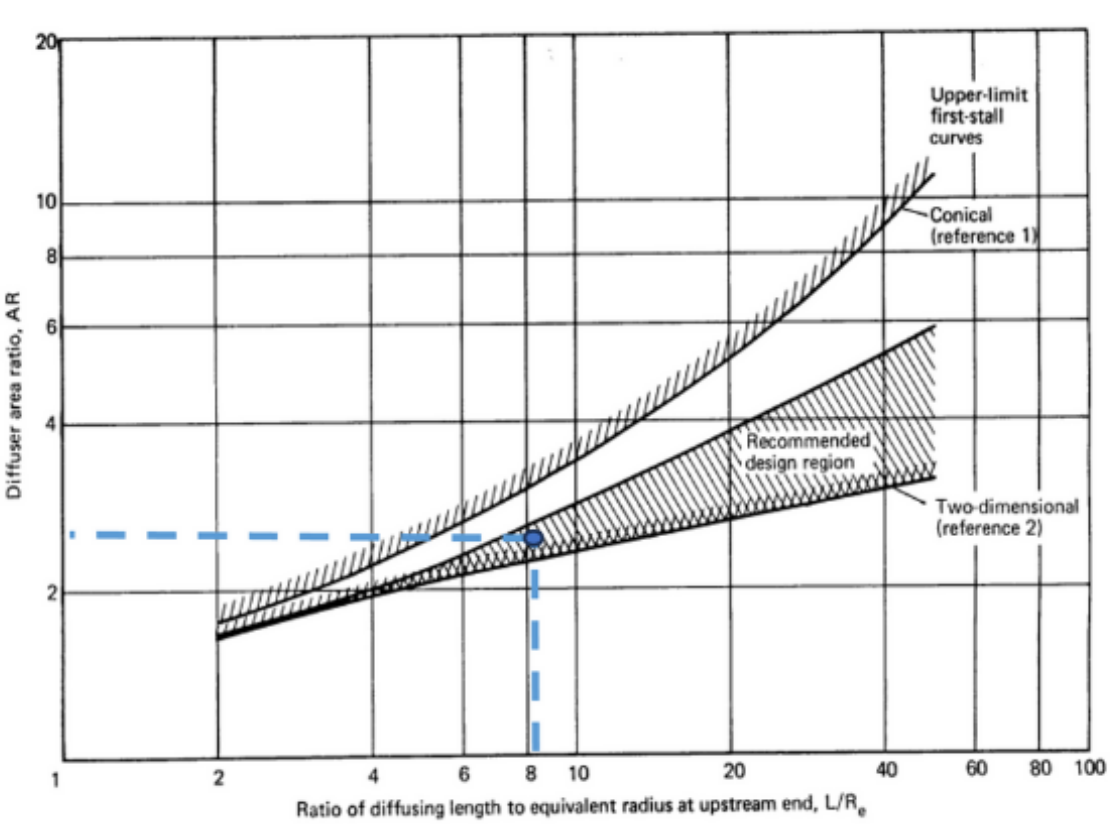

Figure 2.12: Recommended design region for 2D or conical diffusers. Modified from: [24]

2.2.4. Honeycomb

The concept of flow straighteners, colloquially known as honeycombs, traces its roots back to the pioneering work of Prandtl nearly a century ago. These devices serve a pivotal role in guiding airflow in a meticulously controlled manner within wind tunnel systems. Their primary function involves the elimination of undesirable vortices around the tunnel entrance, redirecting the flow axially. This strategic manipulation of the airflow contributes to the stabilization of the overall flow field and effectively curtails the propagation of instabilities.

Figure 2.13 illustrates the diversity of geometric cross-sections that flow straighteners can adopt. Notably, circular cell configurations are recognized as particularly effective in achieving optimal performance. Despite this, hexagonal cell structures have gained prominence as the preferred choice

due to their practical ease of manufacture. The recommended parameters for these elements include a length-to-diameter ratio falling within the range of 6 to 8, coupled with a desired porosity (β) level of approximately 0.8. Such specifications aim to ensure that the coefficients of loss remain below 0.5, as outlined in studies such as [1]. This underscores the critical role played by flow straighteners in enhancing the efficiency and reliability of wind tunnel operations.

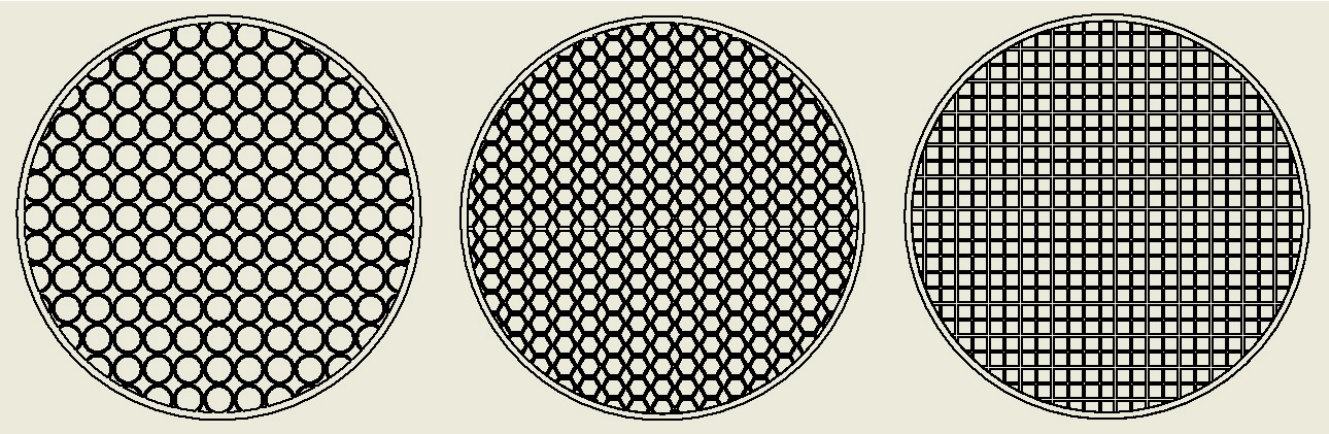

Figure 2.13: 4 Types of honey combs. Source: [Author]

2.2.5. Screens

Their function is to equalize the flow velocity, making them crucial components in a wind tunnel by helping to maintain a uniform velocity profile inside the tunnel. When multiple screens are used, the pressure loss is calculated as the sum of the individual losses from each one [1].

One of the disadvantages of these screens is their porosity, which can lead to the accumulation of dust, counteracting their effectiveness. This issue becomes more pronounced when trying to visualize the flow through a gas. Hence, it is recommended that these screens be removable for easy cleaning [1]. It is important to place these screens within a rigid frame, and the material of the screens should also be rigid, as any flexing can negatively impact the boundary layer [27]. The porosity (β_s)is given by equation 2.7 and it must be between 0,5-0,8.

$$\beta_s = (1 - d_w * \frac{1}{w_m})^2 \tag{2.7}$$

Where d_w is the distance from each cell and w_m is the thickness.

2.2.6. Fan

This component is responsible for driving the fluid through the wind tunnel and dictates the speed within the test section. It is one of the most important parts because the power of the fan ultimately determines the speed achieved in the test section. Care must be taken to isolate this part from the rest of the structure, as vibrations generated by the fan can propagate to other parts of the tunnel, generating noise inside or affecting the accuracy of measurements.

The position of the fan varies depending on the type of wind tunnel. In an induced wind tunnel, the fan is located at the outlet of the diffuser, and its function is to ensure that air flows from the contraction through the entire tunnel, acting as an extractor. In a blow-down wind tunnel, the

fan is positioned before the contraction section, pushing air from the diffuser into the contraction zone.

It is important that the connection between the fan and the diffuser be as smooth as possible to prevent abrupt changes in the cross-section, which can create adverse pressure gradients and cause turbulence inside the diffuser, altering the flow behavior. For this reason, when the diffuser outlet is rectangular, a connecting section is used between the diffuser and the fan. This largely depends on the design of the tunnel.

2.3. Pressure and Pressure loss

Under the assumption of an incompressible, Newtonian, and steady flow, the energy equation in terms of pressure (including losses) is used to estimate the pressure difference (ΔP) between two analysis points ($i-1$) and (i). This is expressed as seen in equation 2.8 where ρ is the air density, V represents the velocity at the respective points, that can be calculated using equation 2.1, and ΔP_{losses} accounts for the local pressure losses in the system.

$$\Delta P = \rho \cdot \frac{V_{i-1}^2 - V_i^2}{2} - \Delta P_{\text{losses}} \tag{2.8}$$

In internal ducts there is always a loss of pressure due to friction between the air and the walls, contractions and expansions of flow, obstruction and also due to its length. These pressure losses (h_f) can be found with the equation 2.9 that is the Darcy-Weisbach equation, where the friction factor (f) is obtained from the equation of Colebrook-Haaland in equation 2.10

$$h_f = \frac{\Delta P_{\text{losses}}}{\rho g} = k * \frac{v^2}{2g} = f * \frac{l}{D_d}\frac{v^2}{2g} \tag{2.9}$$

$$\frac{1}{\sqrt{f}} = -1{,}8log(\frac{6{,}9}{Re_d} + (\frac{\epsilon}{3{,}7D_d})^{1{,}11}) \tag{2.10}$$

Where ϵ is the rugosity of the material used, k is a loss coefficient, g is the gravity force, D_i is the diamter in the section d and Re_d is the Reynolds number in section d. In addition to this equation the friction factor can also be found using the Moody chart but the equation is more precise. [4]

There are also other type of losses for each section present in the wind tunnel, calculated as a pressure loss factor (k) which varies according to the section.

2.4. Velocity Profile

The ideal velocity profile in an empty test section should be parallel to the wind tunnel's symmetry axis and normal to the cross-sectional area. This ideal profile holds except for the region in proximity to the walls, where the velocity should be zero, gradually increasing until it stabilizes. According to Barlow, the variation in the test section should have an average velocity variation between 1 % and 3 % . below 1 % for high-quality aerodynamics testing facilities, while practical applications may range up to 3 %[1].

The first requirement to meet is a steady flow or as close to steady as possible, understanding that achieving perfect steadiness is practically impossible. Nonetheless, steady flow is the desired state because non-steady flow implies boundary layer separation at some point. It is important

to emphasize that this flow separation begins when the wall shear stress equation (τ) seen in equation 2.11 equals zero and increases as its negative value grows. This equation is formed by the flow viscosity and the velocity gradient. Due to viscous forces, the portion of a fluid in contact with a flat plate as it flows matches the velocity of that plate. In this case, the walls of the wind tunnel serve as the flat plate and remain in a static state, resulting in zero velocity of the flow in contact with the tunnel walls. From this point downwards, the flow velocity gradually increases until the inertial forces of the flow surpass the viscous forces, reaching the developed flow velocity. A boundary layer thickness always exists throughout the tunnel; however, boundary layer separation should not occur in the test section but rather at some point in the diffuser so as not to affect the development of the fluid in the test section.

$$\tau = \mu \frac{du}{dy} \tag{2.11}$$

where μ is the rugosity of the material and $\frac{du}{dy}$ is the pressure gradient.

One way to estimate the velocity profile in the test section of a wind tunnel is by measuring the dynamic pressure. It can be done with a static Pitot tube or a hot wire anemometer. This measure has to be done at different velocities at each possible position of the transversal section. However a good approximation due to symmetry is to measure points in the principal axes. Using the relationship of the dynamic pressure with the velocity, this velocity should develop a profile as seen in figure 2.14. These results could be compared with the results obtained from a simulation on CFD, where it is easier to get information from more points but due to symmetry a quarter of the tangential section can be simulated with a turbulence model [28].

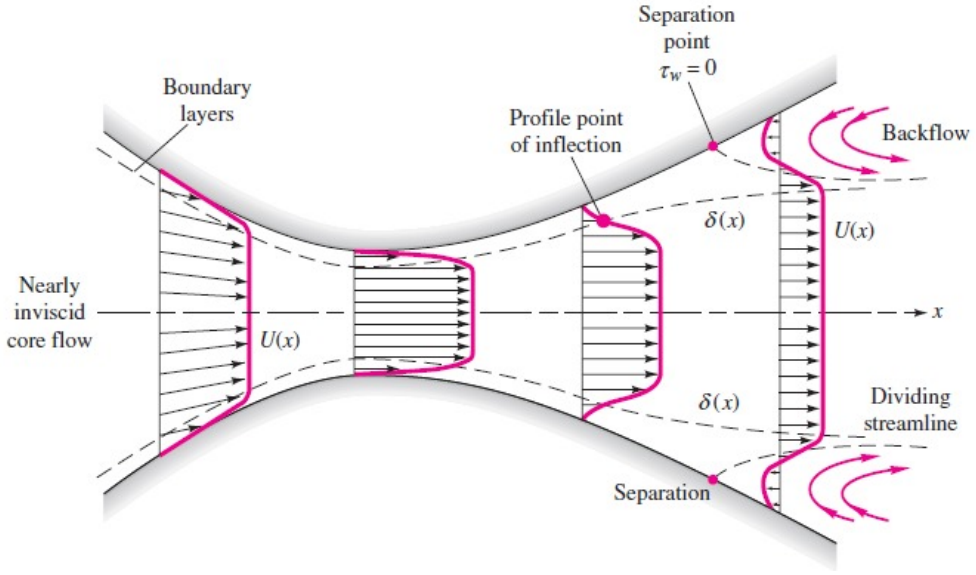

Figure 2.14: Velocity profile throughout a wind tunnel. Source: [4]

3.Design and Construction

In this chapter, the design parameters of the wind tunnel and its structure will be described, mentioning the materials used and the way they were assembled. The machines or tools that were utilized to achieve the required shapes for the wind tunnel will also be specified. Additionally, some properties of the materials and the reasons for their selection will be discussed, as well as the total construction time. Following this, each part will be detailed, with a focus on the dimensions and geometries of the actual pieces built for the wind tunnel. For each section, the calculation procedure for losses will also be shown. Real images of the welded A36 steel structures will be provided, highlighting details within these structures, as well as the circuit constructed to vary the fan speeds. Finally, an image of the completed wind tunnel will be shown, allowing for comparison with the design model presented at the beginning of this section.

The design of this wind tunnel was oriented towards accessibility and repeatability, with the goal of enabling anyone, based on the information provided in this thesis, to reproduce it without complications. Following this goal, a modular design was established where the sections are connected by flanges. A test section is provided to allow for the evaluation of different experiments where velocity measurements can be taken across the entire plane at the central and entrance. Also, the diffuser has the option to take pressure measurements along it every 10 cm to observe pressure losses. This design ensures the wind tunnel can accommodate various experimental setups, making it an ideal tool for academic purposes. Note that in figure 3.15, just 1/4 of the honey comb is shown. This is because it takes to many computational resources to compile the full section.

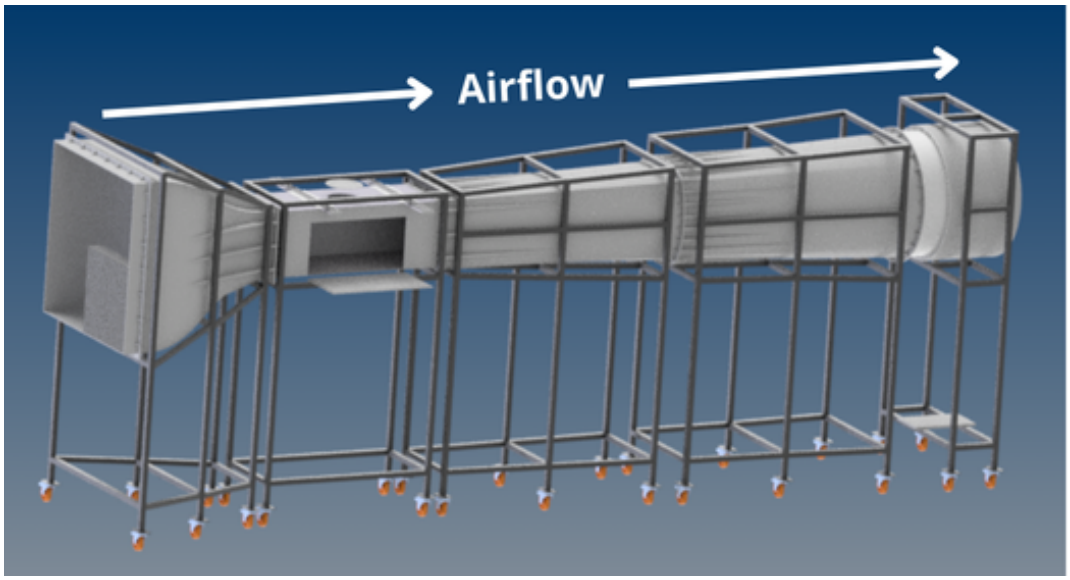

Figure 3.15: Wind tunnel CAD geometry. Source: [Author]

To achieve this design proposed, the design was based on the theoretical framework mentioned earlier, and the system was dimensioned to its maximum capacity delivering 40 m/s in the test section. However, the current fan available for this work can only achieve a maximum speed of 20 m/s in the test section. Therefore, the simulations and pressure calculations that will be shown later are based on a velocity of 20 m/s.Furthermore, for design purposes, screens were included in the design, which are positioned before the honeycomb section. However, this part is not evaluated in this project, and it is left to the user discretion whether to utilize them or not. Technologies such as 3D printing and laser cut in acrylic were chosen for its construction (figure 3.16. Parts designed in PLA can be easily manufactured using printers with the appropriate dimensions, streamlining the acquisition process. Similarly, the provided blueprints allow for the fabrication of parts from acrylic sheets, ensuring efficient and precise construction. Furthermore, the choice of steel for the tunnel's structure ensures adequate strength to withstand the forces generated during aerodynamic tests. Following this line of accessibility, the modular design facilitates the disassembly of all sections, allowing for quick and easy transportation from one location to another according to the user's needs. This portability feature underscores the versatility and practicality of this wind tunnel, making it a valuable and accessible tool for research and experimentation in various environments.

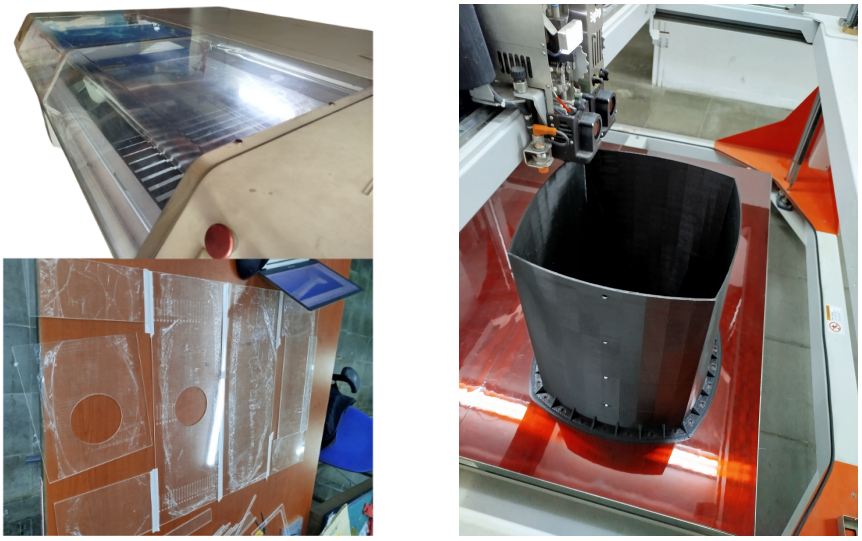

(a) Laser Cutter **(b)** BigRep 3D printer

Figure 3.16: Construction equipments. Source: [Author]

Due to space constraints and the desire for portability, the wind tunnel had to be designed within limited dimensions to avoid exposure. This consideration, coupled with budgetary constraints, led to the decision to create a compact wind tunnel. The primary requirement was that the wind tunnel should be capable of conducting satisfactory experiments on an airfoil profile of up to 20 cm in length. Following Barlow's guidelines for airfoil evaluations, which recommend the length of the airfoil to be up to 80 % of the chord length of the test section, the requirement necessitated a test section with a cross-sectional area of 25 cm x 25 cm. [1]

3.1. Thickness Calculations

Based on the undergraduate project "Simulación aerodinámica y estructural de un túnel de viento modular para la Escuela de Ingeniería Mecánica de la Universidad del Valle"written by Sebastian Rivera an Impetus Indomitus former member. Which provides the design parameters for a wind tunnel with a test section of 50 cm x 50 cm x 1m and a maximum velocity of 50 m/s. The thickness of the wind tunnel sections were designed. Although additional reinforcement was necessary to provide rigidity to the structure, as the internal pressure tends to exert a force that can cause these surfaces to buckle.

The calculation of sheet thickness for the walls of a wind tunnel ensures its structural integrity under Stagnation pressure in the most critical position which is located in the smallest section because the flow velocity is maximum in this region due to the conservation of volumetric flow rate. This pressure generates the greatest forces on the walls, so the tunnel must be designed to withstand this critical condition.

The wind tunnel considered here has a rectangular test section measuring 0,25 m × 0,25 m, a diffuser that transitions to a circular exit with a diameter of 0,46 m, and a contraction zone. The materials used are acrylic for the test section and PLA for the contraction and diffuser which propierties can be seen in table 3.1.

The Stagnation pressure in the smallest section, which corresponds to the test section, is calculated using Bernoulli's equation using the maximum velocity obtaining a maximum differential pressure of 236.8 Pa and with a static pressure assumed as the atmospheric pressure at 24 °C of 101365 Pa. Using equation 2.4, P_{Stg} is 101570 Pa. Although the velocity and dynamic pressure decrease in the diffuser and larger sections, designing for the highest pressure ensures the structure's safety and reliability.

$$t = \frac{P \cdot D}{2 \cdot \sigma_{allowable} \cdot FS} \tag{3.12}$$

where: D = 0.25 m, is the hydraulic diameter, FS=2 is the security Factor and $\sigma_{\text{allowable}} = \sigma_{\text{fluency}}/FS$ is the allowable stress, with FS = 2 as the safety factor since the load conditions are predictable. This margin is sufficient to prevent critical deformations and ensure flow stability.

Since for acrylic the yield stress is $\sigma_{\text{fluencia}} = 80\,\text{MPa}$, so $\sigma_{\text{allowable}} = 40\,\text{MPa}$. Substituting these values in equation 3.12 gives the following result:

$$t_{\text{acrylic}} = \frac{101570 \cdot 0{,}25}{2 \cdot 40 \times 10^6} = 0,32\,\text{mm}. \tag{3.13}$$

For PLA in the contraction and diffuser, the yield stress is $\sigma_{\text{fluencia}} = 70\,\text{MPa}$, so $\sigma_{\text{allowable}} = 35\,\text{MPa}$. Substituting these values in equation 3.12 the equation remains as follows:

$$t_{\text{PLA}} = \frac{101570 \cdot 0{,}25}{2 \cdot 35 \times 10^6} = 0{,}36\,\text{mm}. \tag{3.14}$$

The calculated values represent the minimum thickness required to resist dynamic pressure in the smallest section. Using these values for all sections ensures that the walls can withstand the highest stresses encountered. Although the calculated thicknesses are sufficient to resist the stagnation pressure, a thickness of 3 mm was chosen to have a robust equipment ensuring adequate stiffness and account for potential imperfections or unexpected loads during operation.

3.2. Materials

Having the need for a custom wind tunnel that could be produced quickly and cost-effectively, 3D printing with PLA was selected for the contraction zone, diffuser, and flanges. Acrylic was used for the test section to ensure clear visibility of the objects inside. For the structure, square steel profiles with 2 cm edges and 1 mm thickness were chosen, providing an optimal balance between lightness and rigidity. These steel profiles are robust enough to withstand aerodynamic loads and support the weight of the wind tunnel sections, while their reduced thickness helps to minimize the overall weight of the structure.

In addition Plastic straws OF Polypropylene (PP) were used to create the honeycomb, and Medium Density Fiberboard (MDF) was utilized for the transition between sections, along with latex to ensure smooth airflow. To connect the sections, pieces of foamy material were employed to prevent leakage. And finally, to secure the wind tunnel to the structure without causing damage Polyurethane (PU) foam was used throughout to facilitate easier handling and assembly of the modular wind tunnel, without compromising stability and precision, ensuring reliable measurements during testing. In Table 3.1, the materials, construction methods, and some properties of the materials for each section can be seen. Additionally, the time taken for the construction of these components and their weight are also provided.

Table 3.1: Wind Tunnel Materials, Components, and Specifications

Section	**Material**	**Construction Method**	$\boldsymbol{\rho}$ [Kg/m^3]	$\boldsymbol{\sigma_y}$ [MPa]	$\boldsymbol{\epsilon}$ [μm]	**Time** [hrs]	**Weight** [kg]
Honeycomb	PP PLA	Assembly	910 1240	80,0 70,0	0,2 9,1	336	0,820
Contraction	PLA Foamy	3D Printing	1240 30	70,0 0,2	9,1 1,5	96	4,265
Test Section	PMMA PLA	Laser Cutting	1200 1240	80,0 70,0	0,2 9,1	5	2,342
Diffuser	PLA Foamy	3D Printing	1240 30	70,0 0,2	9,1 1,5	192	9,242
Fan Transition	MDF Latex PLA Foamy	Manual Cutting	700 930 1240 30	20,0 25,0 70,0 0,2	6,0 0,2 9,1 1,5	6	3,250
Structure	Steel Profiles PU Foam	Welding	7850 100	600,0 0,3	0,2 2,0	504	14,448

A 3 mm thick acrylic sheet was selected for the test section of the wind tunnel due to its outstanding features. Its transparency allows clear visualization of the airflow, while its impact resistance ensures structural integrity during experiments. Furthermore, its ease of machining facilitates manufacturing according to tunnel specifications, and its availability and reasonable cost make it a practical choice compared to other transparent materials [29].

Due to the dimensions of the parts, a Big Rep printer was used, with printing capacities of up to 1 cubic meter. 2.85 mm filament from 4D Lab was employed, supported by its technical datasheet [30]. However, the selected printing orientation, perpendicular to the 3D printing lines, can generate a surface roughness of up to 32.78 μm as demonstrated in previous studies [31]. This

orientation also affects tensile strength by up to 36 %, which is important to consider in the design and evaluation of printed parts [32].

With all this, the estimated total construction time for the wind tunnel is 1,139 hours, and the approximate total weight is 29.173 kg, plus an additional 8.900 kg for the fan, giving a total of 38.073 kg. This shows that it is a very lightweight tool, perfect for transport, while also providing stability on the ground.

3.3. Fan Parameters

When selecting a fan for a wind tunnel, it is essential to consider several parameters to ensure proper airflow through the test section. Key factors include air volume flow rate, pressure generation, power consumption, and efficiency. A suitable fan should provide enough airflow to reach the required airspeed without introducing unwanted flow disturbances. Additionally, it should operate at optimal efficiency to minimize energy losses and ensure stable performance. Finally, it is important to control its velocity so experiments can be hold precisely.

The fan chosen for this wind tunnel is an ziehl-abegg fan and the reference is ZN045-6IL.BD.V7P2 ZAplus axial fan with sickle blades seen in figure 3.24e. This fan operates with a voltage range of 200-277V, with a power rating of 1420W and a maximum speed of 1470 RPM, enabling it to handle airflows up to 4485 m^3/h with a pressure increase of 160 Pa. Its energy efficiency is 57.1 %. This fan offers a robust and efficient solution for the wind tunnel, ensuring consistent and controlled airflow for experimental purposes. This fan was selected due to its quiet operation, low power consumption, high stability with minimal vibrations, and, ultimately, because it was donated to the research team.



(a) Frontal View (b) Rear View

Figure 3.17: Frontal and rear views of the wind tunnel fan. Source[Author]

3.4. Test Section

A multifunctional test section was designed for various purposes, one of which is the evaluation of airfoils. This section allows for the connection of aerodynamic balances and the rotation of objects to the necessary angles, providing flexibility for different testing scenarios. It is configured to take dynamic pressure data across the entire plane of the cross-section: the first measurement

plane is located in the middle of the section, and the second at the junction between the contraction zone and the test zone.

The test section features high-precision instrumentation and a modular design, enabling easy adjustments to accommodate different setups. Advanced sensors and data acquisition systems are integrated to capture high-frequency fluctuations in dynamic pressure across the entire plane, enhancing measurement quality. Additionally, visualization tools, such as high-speed cameras and smoke generators, provide a comprehensive understanding of flow patterns around the test objects, making this section a versatile tool for aerodynamic research and development.[25].

To perform data collection across the entire cross-section, a mechanism was devised to slide the measuring tool, in this case, the static Pitot tube, along a vertical line in the XY plane, moving in the Y direction. This design prevents any air leakage during movement. This system can be seen in Figure 3.18. In image a, there is an aperture through which the static Pitot tube is inserted. This piece has freedom of movement along the Y-axis of the image, allowing it to cover the entire d_{hTs}25 cm edge. In image b, the detail is shown from the front view of the test section, where two white pieces that make up the clamping system are visible.

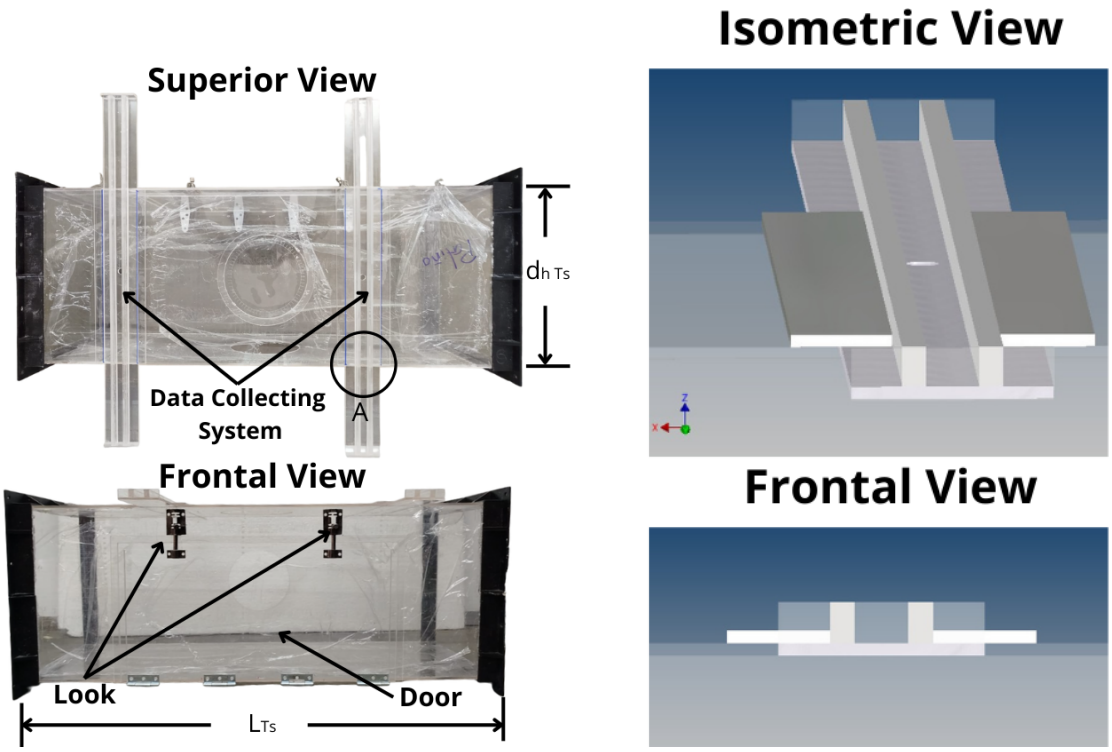

(a) Test section built **(b)** Detail A

Figure 3.18: Test section: (a) test section built and (b) Detail A. Source:[Author]

Regarding the length of the section, it was established to be L_{Ts}=70 cm in order to achieve fully developed flow and to have a longer test section. The bibliography indicates that it should be more than twice its edge length, so a longer length was chosen to ensure well-developed flow, ensuring that this value is within the permitted limits. [1]

3.4.1. Pressure losses in Test Section

As the cross-sectional area of this section is constant, using Equation 2.1, the inlet velocity is the same as the outlet velocity, meaning that the pressure losses are only due to local losses, ΔP_{Ts}. As previously described, equation 4.47 is used to determine the friction factor, which in turn is used to calculate the pressure loss factor through equation 2.9. However, the Reynolds number must first be determined.

$$Re = \frac{vD\rho}{\mu} = \frac{\left(20\frac{\text{m}}{\text{s}}\right)(0{,}25\text{ m})(1{,}184\text{ kg/m}^3)}{1{,}849 \times 10^{-5}\text{ N.s/m}^2} = 320173,066 \tag{3.15}$$

$$\frac{1}{\sqrt{f}} = -1{,}8log(\frac{6{,}9}{320173,066} + (\frac{0,2 * 10^{-6}}{3,7 * 0,25})^{1,11}) \tag{3.16}$$

$$h_{fts} = 0,002120 * \frac{0,7}{0,25}\frac{20^2}{2 * 9,81} = 0,121m \tag{3.17}$$

$$\Delta P_{T.S.} = 1,406Pa \tag{3.18}$$

3.5. Honeycomb

The effectiveness of a honeycomb structure is evaluated based on its porosity and the length-to-diameter ratio of the cells, which impact its ability to straighten flow and minimize turbulence. In this case, the straighteners were made from plastic straws, cut to specific dimensions to meet the previously mentioned conditions. They were attached with silicone. Although this was a time-consuming process, it ensured the desired structure, and for small-scale wind tunnels, this method can be used and will yield good results [1].

To create a honeycomb structure straws with a 7 mm external diameter (D_{hc}), and a thickness (T_{hc}) of 0,1 mm and 5 cm length (L_{hc}) were used, as this configuration guarantees a porosity of 0.975. This measurement is obtained by dividing the transversal area occupied by the 4874 straws over the total transversal area. Additionally, the chosen straws provide a length-to-diameter ratio of 7.14 , which are the design parameters specified in Section 2.2.4. These parameters ensure optimal flow conditioning for the wind tunnel, reducing turbulence while maintaining sufficient airflow through the honeycomb. This arrangement can be seen in figure 3.19

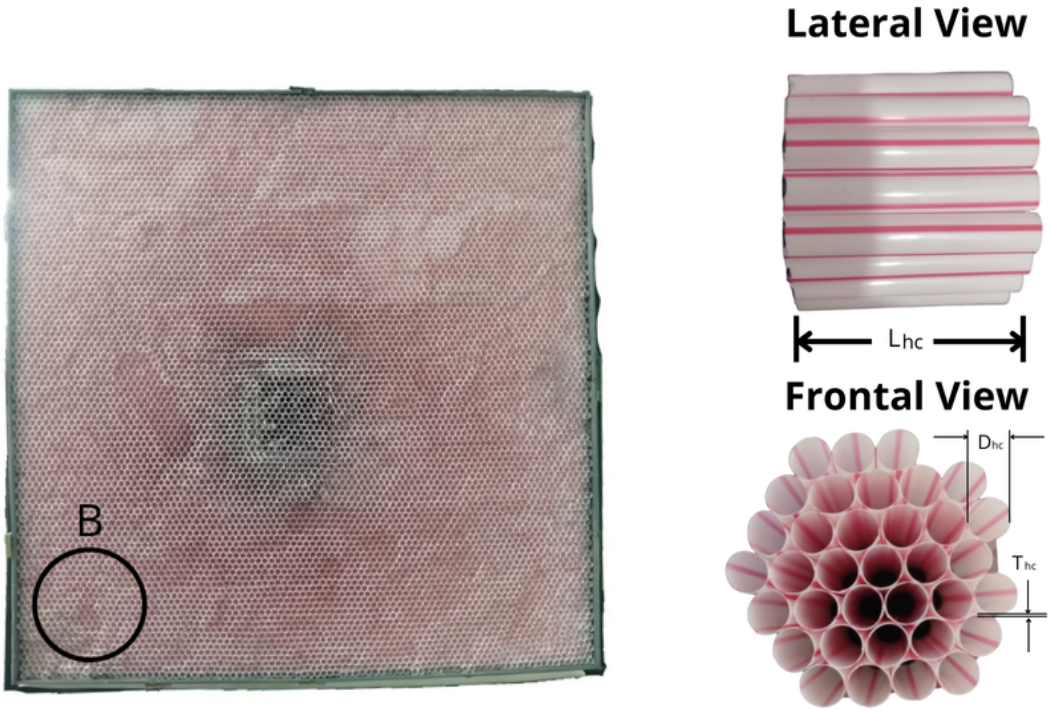

(a) Honeycomb arrangement **(b)** Detail B

Figure 3.19: Honeycomb photo and (b) Detail B. Source: [Author].

3.5.1. Pressure losses in Honeycomb

To calculate the losses in the honeycomb, the same principle applies as in the test section, since the cross-sectional area is constant. Therefore, the losses are due to local losses only.The same equation is used, and the pressure loss coefficient in the honeycomb (K_{hc}) is obtained as shown in equation 3.19, where λ_{hc} is defined in equation 3.20 and ϵ represents the straws roughness.

$$K_h = \lambda_h \left(\frac{L_h}{D_h} + 3\right)\left(\frac{1}{\beta_h}\right)^2 + \left(\frac{1}{\beta_h} - 1\right)^2 \tag{3.19}$$

$$\lambda_h = \begin{cases} 0{,}375\left(\frac{\epsilon}{D_h}\right)^{0,4} Re_\epsilon^{-0,1} & \text{for } Re_\epsilon \leq 275 \\ 0{,}214\left(\frac{\epsilon}{D_h}\right)^{0,4} & \text{for } Re_\epsilon > 275 \end{cases} \tag{3.20}$$

$$h_{fhc} = 1,234 * \frac{2,958^2}{2 * 9,81} = 0,55m \tag{3.21}$$

$$\Delta P_{H.C.} = 6,392Pa \tag{3.22}$$

The pressure loss coefficient for circular channels in the honeycomb (K_{hc}), when the ratio of hydraulic diameter to length is 6, is 0.3 [1]. However, as in this case, the ratio is 7.14, within the acceptable range, the previous equation is used to determine this value, resulting in 0.346 Pa.

For this case, the straighteners were made from plastic straws, which were cut to the necessary dimensions to meet the previously mentioned conditions. They were adhered with cold silicone, a process that, although time-consuming, ensured the desired structure. For small-scale wind tunnels, this method is feasible and can yield good results [1].

3.6. Contraction zone

As established in subsection 2.2.1, a fifth-order polynomial is the most suitable for achieving the desired fluid behavior inside the wind tunnel. For this reason, this profile was selected to design the contraction section. Also fulfilling with the design criteria in that section and following what it said by Barlow [1] the total length (L_C) is 65 cm and the total edge length ($2H_i$) is 65 cm too in order to achieve an are ratio (AR) of 0.148, value that is admissible. Since it was 3D-printed, guide ribs were added to provide rigidity and prevent buckling due to internal pressure. These ribs are shown in figure 3.20 and they enhance the structural integrity of the design, ensuring that it remains stable under operating conditions.

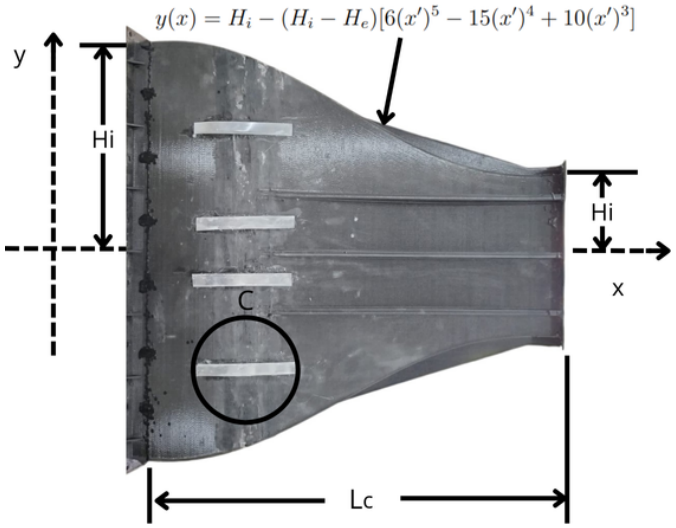

Figure 3.20: Contractor dimensions. Source: [Author]

In Figure 3.20, four aluminum sheets as the one in detail C can be seen adhered to the surface of the contractor. This was due to complications in the manufacturing of this piece. The part had a printing time of 4 days. During the printing process, the electrical grid at the Machine-Tool Workshop at Universidad del Valle, where this piece was been printed, experienced frequent power shutdowns. Although the 3D printer was connected to a UPS, it only provided 30 minutes of backup power. When the power would go out, instead of losing the material and the time invested in the print so far, a redesign was implemented. The printing process was paused, and the height of the printed section was measured. Using this measurement, the remaining section was printed separately and then joined with epoxy weld, sanded, and smoothed to ensure the internal surface was even. In this particular case, the print failed before reaching the proper guides that provide rigidity, so aluminum sheets were used to add strength. This kind of issue occurred more than once with different parts, so this method was also applied to the diffuser.

3.6.1. Pressure losses in the contraction zone

To calculate the losses in the contraction zone, Se calcula la velocidad estimada a la entrada usando la ecuacion 2.1 y se encuentra la presión como se ve en la ecuacion 3.23

$$\begin{aligned}\Delta P_c &= \frac{\rho}{2}\left(V_{\text{out}}^2 - V_{\text{in}}^2\right) + \Delta P_{\text{Losses C.}} \\ &= \frac{1{,}184}{2}\left(20^2 - 2{,}96^2\right) + \Delta P_{\text{Losses C.}} \\ &= 231{,}62\,\text{Pa} + \Delta P_{\text{Losses C.}}\end{aligned} \tag{3.23}$$

The pressure loss coefficient (K_{cz}) is obtained as shown in equation 3.24. However the term in the integral can be summarize by 0.32 as seen in equation 3.25 and the friction factor used is the average (f_{sv}) along the section [1].

$$K_n = f_{av}\left(\frac{L_c z}{D_{ts}}\right)\int_0^1 \frac{D_{ts}}{D_x} d\left(\frac{x}{L_n}\right) \tag{3.24}$$

$$K_{nl} = 0{,}32 f_{av}\frac{L_{cz}}{D_{cz}} \tag{3.25}$$

$$h_{fcz} = 0,004 * \frac{2,958^2}{2 * 9,81} = 0,086m \tag{3.26}$$

$$\Delta P_{LossesC.} = 1,03Pa \tag{3.27}$$

D_{ts} is the hydraulic diameter in the test section and D_x is the hydraulic diameter along the contraction zone. For this case the pressure loss coefficient (K_{cz}) is 0,004 and the local pressure loss is 1,03 Pa. Therefore the total Pressure loss is ΔP_c is -232.65 Pa.

3.7. Diffuser

To minimize the abrupt change from a rectangular to a circular section exiting the fan, it was established that the diffuser should have a rectangular inlet and a circular outlet with an opening angle (θ) of 3.01°. Furthermore, this type of changing cross-section along the length of the diffuser (L_d) provides a gradual and uniform transition of the airflow entering the wind tunnel. This reduces turbulence and improves flow uniformity. Additionally, since this piece was constructed using 3D printing, its manufacturing was not as complicated as it would be with other methods. the only inconvenient was to separate the difuser in two parts because of the 3-D printer size.

Considering the inlet hydraulic diameter (D_{hid}) of the diffuser, which must be the same the test section, and the exit hydraulic diameter (D_{hed}), considering the extractor with a diameter of 46 cm. Then it must be the same.On the other hand taking into account the valid ranges for AR= 2.659 and RE=8.522 illustrated in figure 2.12, the proposed dimensions of the diffuser are shown in the figure.3.21

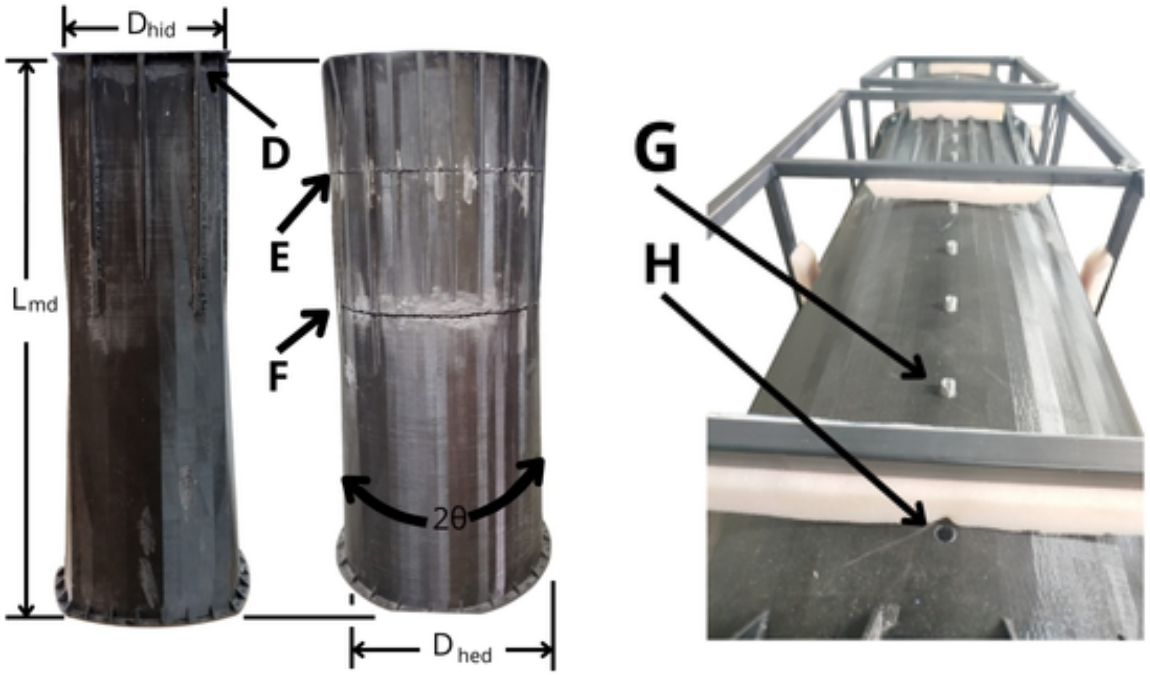

(a) Diffuser dimensions **(b)** Pressure tap fittings

Figure 3.21: Diffuser details: (a) Diffuser dimensions and (b) Pressure tap fittings. Source: [Author].

The total length of this part is 1.96 meters, which exceeds the printing capacity of a single print on the 3D printer. Consequently, the section was subdivided into two half lengths (L_md) of 98 cm parts to allow for full 3D printing. Similar to the contraction zone, this section is reinforced with an external structure designed to strengthen it, ensuring that the internal pressure generated within the wind tunnel does not cause excessive deflection of the material. Additionally, due to recurring electrical issues, the 3D printer stopped at specific points (D, E, and F). However, as was done with the contraction zone, the parts were realigned and joined using epoxy welding, ensuring that the internal surface remained smooth. Although this process required additional effort, it successfully maintained the integrity of the diffuser.

Furthermore, along the entire length of the diffuser, there are holes (indicated by G) spaced 10 cm apart. These were incorporated to facilitate pressure measurements and to characterize the velocity profile along the diffuser. When not in use, these holes are sealed with plugs similar to the one shown at point H, ensuring the diffuser remains airtight during operation.

3.7.1. Pressure losses in Diffuser

Using equation 2.1, it is found that the exit velocity is 7.52 m/s, therefore:

$$\begin{aligned} \Delta P_D &= \frac{\rho}{2}\left(V_{\text{in}}^2 - V_{\text{out}}^2\right) + \Delta P_{\text{losses D.}} \\ &= \frac{1{,}184}{2}\left(20^2 - 7{,}52^2\right) + \Delta P_{\text{losses D.}} \\ &= \frac{1{,}184}{2}\left(400 - 56{,}5504\right) + \Delta P_{\text{losses D.}} \\ &= 203{,}5 + \Delta P_{\text{losses D.}}\,\text{Pa} \end{aligned} \tag{3.28}$$

Because the diffuser section varies, it conformed by the sum of two types of losses: friction losses and expansion losses, determined by friction losses coefficient (k_f) and expansion losses coefficient (k_{ex}) seen in equations 3.29 and 3.30[1]. The factor $K_e(\theta)$, where (θ) is the opening angle, is very influenced by the sectional area and there are values depending in the angle determined by [33]. These values for square and circular cases can be seen in equation 3.31and 3.32 and for difuser that change from rectangular to circular a mean between two cases is acceptable [1].

$$K_f = \left(1 - \frac{1}{A_R^2}\right) \frac{f}{8 \sin \theta} \tag{3.29}$$

$$K_{\text{cx}} = K_e(\theta) \left(\frac{A_R - 1}{A_R}\right)^2 \tag{3.30}$$

$$K_{\text{e(circle)}} = \begin{cases} 0{,}1033 - 0{,}023890 \text{ for } 0 < \theta < 1{,}5^\circ \\ 0{,}1709 - 0{,}11700 + 0{,}03260\theta^2 + 0{,}001078\theta^3 \\ -0{,}0000076\theta^4 - 0{,}00001331\theta^5 + 0{,}00001345\theta^6 \\ \text{ for } 1{,}5^\circ \leq \theta \leq 5^\circ \\ -0{,}09661 + 0{,}046728 \text{ for } 5^\circ < \theta \end{cases} \tag{3.31}$$

$$K_{\text{e(square)}} = \begin{cases} 0{,}09623 - 0{,}0041520 \text{ for } 0 < \theta < 1{,}5^\circ \\ 0{,}1222 - 0{,}045900 + 0{,}02203\theta^2 + 0{,}003269\theta^3 \\ -0{,}0006145\theta^4 - 0{,}00002800\theta^5 + 0{,}00002337\theta^6 \\ \text{ for } 1{,}5^\circ \leq \theta \leq 5^\circ \\ -0{,}01322 + 0{,}058660 \text{ for } 5^\circ < \theta \end{cases} \tag{3.32}$$

Using these equations taking into account that AR is 2,66, RE is 8,51 and θ is 3° then The losses factor (K_d) is 0,472 and the pressure losses for diffuser (h_{fd}) is 113,843 Pa

$$h_{fcz} = 0,472 * \frac{2{,}958^2}{2 * 9{,}81} = 9{,}81m \tag{3.33}$$

$$\Delta P_{LossesD.} = 113{,}846Pa \tag{3.34}$$

3.8. Fan transition

This section connects the diffuser outlet with the fan. Typically, vortices are created in the corners of this section because the diffuser is usually rectangular while the fan has a circular cross-section, requiring a coupling that is rectangular on one side and circular on the other. This can lead to areas of adverse flow, which may negatively affect the downstream flow. To address this, the diffuser was designed with a rectangular inlet that connects to the test section, gradually transitioning to a circular shape, enabled by a 3D printer. A wooden section was designed to fit the fan end, an internal latex material was used to prevent vibration transfer from the fan to the rest of the tunnel and a PLA ring to connect to the diffuser as shown in Figure 3.22. Also Foamy was also used between sections to mitigate even more, the vibrations

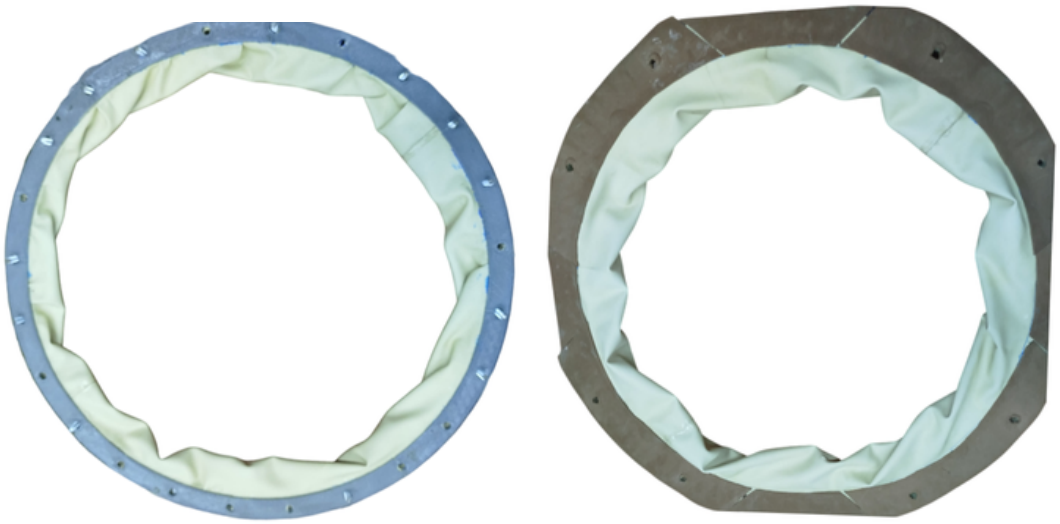

(a) Diffuser part coupling **(b)** Fan coupling part

Figure 3.22: Fan-diffuser transition. Source: [Author]

3.9. Theoretical Pressure losses

The pressure losses identified in each section of the wind tunnel were collected based on the specific design parameters established earlier. This process involved gathering data from critical components such as the honeycomb, test section, contraction zone, and diffuser to thoroughly evaluate the pressure losses within each of these sections. The inclusion of these sections allows for a comprehensive understanding of how pressure is distributed and lost as air moves through the tunnel. Additionally, it is important to note that when an object is placed within the wind tunnel for testing, the pressure loss resulting from its presence must be factored into the analysis, as this loss can be substantial. Objects in the test section alter the flow, generating additional turbulence and resistance, which lead to further energy loss that can impact the accuracy of aerodynamic evaluations. In Table 3.2, the collected data on these pressure losses are presented.

Table 3.2: Pressure losses in wind tunnel

Section	$\Delta P_{Losses}[Pa]$
Test Section	1.406
Honey Comb	6.392
Contraction Zone	232.620
Diffuser	113.856

This data serves as a basis for evaluating the design parameters and will later be compared with simulation results to assess the model's predictive accuracy and the tunnels operational efficiency. Through this analysis, it becomes possible to identify areas for improvement and adjustments in the wind tunnel's setup to optimize testing conditions for future experiments.

3.10. Control Circuit

To control the airflow velocity, the speed regulator circuit in figure 3.23 was designed and implemented. The circuit was integrated with the fan to allow for adjustable speeds, ensuring that the wind tunnel could operate at various airflow rates depending on the testing requirements. The electrical connections were carefully set up, allowing smooth transitions between different speeds, thereby enhancing the versatility and performance of the wind tunnel.

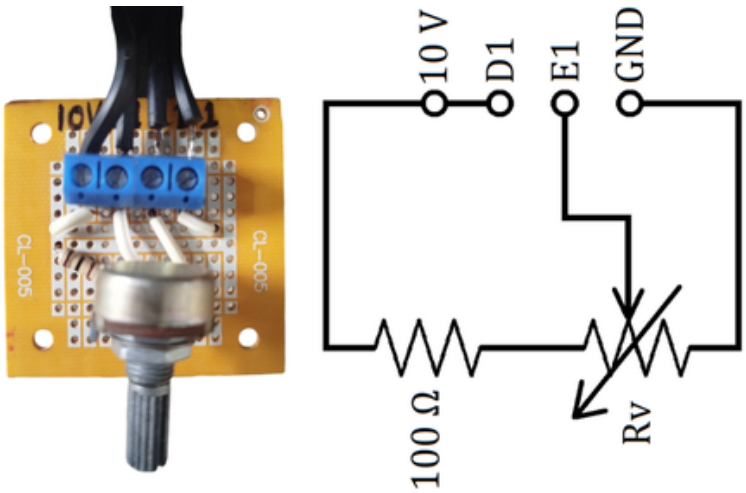

Figure 3.23: Real velocity control. Source: [Author]

The internal circuit of the fan supplies a 10V input to this circuit, allowing for adjustable voltage at the output point (E1) by setting the potentiometer (Rv). The diode (D1) is included to protect the components at the output from reverse polarity or voltage spikes, allowing current to flow in only one direction if correctly oriented. The ground connection is marked as GND. A fixed resistor of 100 Ω is included in series to prevent the circuit from burning out and to ensure that there is always some resistance in the circuit, even when Rv is set to zero.

3.11. Structure

A36 steel was selected for the structure, using 6-meter square tubes of 3/4" and 1.1 mm thickness. This material was chosen for its ease of welding and its strength, which is more than sufficient to support the wind tunnel, primarily made of PLA. Additionally, an individual structure was fabricated for each section of the tunnel to maintain the modular functionality. Since the diffuser was printed in two sections there were built two structures too for these parts. The individual structures can be seen in figure 3.24. Considering the length of the diffuser, it was divided into two parts, each with its own structure.



(a) Contraction zone structure **(b)** Test section structure **(c)** Structure diffuser part 1

(d) structure Diffuser part 2 **(e)** Fan structure

Figure 3.24: Structure for supporting the wind tunnel sections. Source [Author]

The structure was designed to be lower in height to minimize the risk of vibrations and to allow the operator to perform analyses while seated, comfortably viewing the necessary operations on their computer. On the other hand, foam was used to ensure that the tunnel components do not come into direct contact with the structure, helping to mitigate vibrations. the disposition of these foams is presented in figure 5.31a.

Each structure was designed with hinges to allow the necessary part to be inserted and secured using self-drilling screws, applying pressure to the component that comes into contact with the foam attached to the structure as seen in figure 3.25b. This setup prevents vibrations while transporting it to different places or ground vibrations while staying put. It also ensures that the part is firmly adjusted and does not slide, keeping it securely in place.



(a) Foam to reduce vibrations and screw coupling

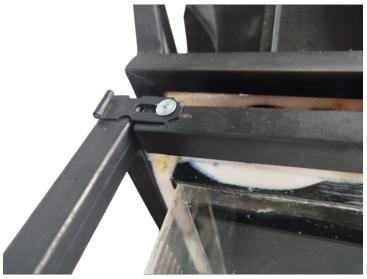

(b) Screw mounting



(c) Locking caster and leveling

Figure 3.25: Structure details. Source: [Author]

To facilitate movement, wheels with locks were attached to each of these structures, allowing them to be easily moved and fixed in place as needed. Furthermore, due to potential unevenness in the surfaces where the tunnel might be placed, these wheels are equipped with a system of four screws that can raise or lower each leg to adjust to the surface. This system is appreciated in figure 5.31b.

3.12. Wind Tunnel Assembly

During the construction phase of the modular wind tunnel, several unforeseen challenges arose that demanded more time and effort than initially planned. One of the most labor-intensive tasks involved assembling the honeycomb structure by bonding plastic straws together using cold silicone. This step was crucial as the honeycomb is responsible for straightening the airflow before it reaches the test section. Despite receiving assistance from a fellow engineering student, the process took several days to complete due to the need for precise alignment and consistent bonding. The task required patience and meticulous attention to ensure the honeycomb was both effective and durable.

The assembly of the wind tunnel required the precise cutting of foam sheets to be placed between each section and the main structure. These foam sheets were essential for minimizing vibrations and sealing gaps between different components. The foam located at the bottom of the tunnel sections had to be at least twice as thick as the other sections, particularly in larger areas, due to the weight compressing the foam. Since the foam is not very dense, it was necessary to ensure that, when the sections were closed, they would be securely clamped in place as seen in figure 3.26. Each piece of foam was cut to dimensions of 6 cm in height and 4 cm in width, with the length varying depending on the area of contact, ensuring a snug fit and preventing unwanted movement or vibrations during operation.



Figure 3.26: Disassembled wind tunnel. Source: [Author]

Each connection between sections also included cut pieces of foamy that were placed along the joint. When the sections were screwed together, this foam would compress and effectively seal any potential air leaks. This step was crucial for maintaining the internal pressure within the wind tunnel, ensuring that there were no unintended pressure losses that could affect the accuracy of the experiments. Proper sealing between sections is vital for consistent and reliable results, as even small leaks could disrupt airflow and lead to measurement errors.

The metal structure was painted using black spray paint to protect it from corrosion and ensure its durability over time, especially when exposed to varying environmental conditions. The steel frame itself was welded by a fellow university graduate, guaranteeing the stability and strength needed to support the wind tunnel's components and withstand aerodynamic forces. However, the process did not end there; the installation of locking caster wheels required drilling holes manually using a power drill. Given the thickness of the floor plate, special drill bits were purchased to handle the material without damaging it. This extra step ensured that the wind tunnel could be easily moved and adjusted as needed, providing flexibility for various experimental setups. Each wheel was fastened to the structure using four bolts, twelve nuts, four standard washers, and four lock washers, ensuring a secure fit that allows for easy movement and stability. The inclusion of these wheels means that the wind tunnel can be adjusted even on uneven surfaces, thanks to the ability to level and stabilize the setup. This adaptability is particularly useful during testing, as it allows the structure to be quickly repositioned or reoriented without compromising the integrity of the setup.

The completion of this process described before brought as result the finished subsonic wind tunnel that can be seen in figure 3.27. The total amount of time for one person to ensemble the wind tunnel from the status in figure 3.26 to 3.27 is approximately 45 minutes using 1 combination wrench.On the other hand the time needed to disarm it is in average only 20 minutes.



Figure 3.27: Real Wind Tunnel. Source: [Author]

4.CFD Simulation

In this chapter, the simulation parameters, selected case, and critical aspects considered to ensure an accurate and reliable simulation process are discussed. Initially, the factors taken into account for setting up the simulation are outlined, including relevant conditions and assumptions associated with the specific case. Following the setup, a mesh independence analysis was conducted to verify that the simulation results remained consistent regardless of mesh size, ensuring that numerical accuracy was maintained. The final mesh chosen for the simulations is presented, demonstrating the balance achieved between computational cost and result precision. Key parameters used in the simulations are also detailed, with simulations performed at different airspeeds of 20, 15, 10 and 5 m/s to analyze the behavior under a range of flow conditions. Additionally, the governing equations for this simulation case are presented, with a focus on the kω-SST (shear stress transport) turbulence model.

4.1. Parameters for CFD Using OpenFoam

To validate the information before starting construction, CFD simulation was conducted using OpenFOAM (Open Field Operation and Manipulation) to obtain the velocity profile data from the simulation and compare it with the experimental data that would be collected later. OpenFOAM is an open-source CFD software used for simulating fluid flow, heat transfer, and associated physical phenomena. It allows users to solve complex fluid dynamics problems using numerical methods. Simulation is a crucial step in this process because it allows for the prediction of flow behavior within the wind tunnel, reducing the likelihood of errors and costly modifications during physical testing. OpenFOAM was chosen for its versatility and open-source nature, which makes it an ideal tool for complex computational fluid dynamics (CFD) simulations.

Before starting, the CAD geometry was selected, and to save computational resources, 1/4 of the symmetric geometry was chosen to run the simulation. Due to its symmetrical nature, the results obtained are suppose to be accurate, as the symmetry planes were appropriately defined as symmetry boundary conditions. This approach ensures that the simulation provides valid results while reducing the computational load, making the process more efficient. Although turbulence is inherently chaotic and irregular, it tends to stabilize when averaged over a period of time. In a symmetric wind tunnel design, it is reasonable to assume that the behavior observed in the simulated section will be comparable to what occurs in the regions that were not simulated [34].

After having designed the geometry, the next step was meshing it. To accomplish this, the mesh must fulfill certain quality parameters to ensure it accurately reflects the real phenomena. These parameters are:

- Skewness: measures the deviation of mesh elements from an ideal shape. A value close to 0 represents an ideal shape, while values approaching 1 indicate highly distorted elements,

which can negatively impact convergence and accuracy.

- Aspect Ratio: the difference between the lengths of the longest and shortest sides of an element. A value of 1 indicates a perfectly equidimensional element, while higher values indicate elongated or flattened elements. it is recomended to be up to 10.

- Non-Orthogonality: The angle between the centroid vector and the unit normal vector measures how well the faces of the mesh elements align with the direction of the variables to be solved, such as flow direction. This value should be less than 70° for OpenFoam and values closer to 1 are preferable as they represent better alignment of the mesh elements with the flow field, reducing discretization errors.

These ranges are critical to maintain because they ensure that the numerical solution converges effectively and that errors due to mesh quality are minimized, leading to reliable results. If these parameters are met, the mesh can accurately capture the flow details required. [35]

In addition to these parameters, the Kolmogorov scale, seen in Equation 4.35, must be respected because it represents the smallest eddies present in the turbulent flow. If the mesh does not resolve this scale properly, it will fail to capture the energy dissipation accurately, which could lead to significant deviations in the simulation results for turbulent flows.

$$\eta = \left(\frac{\nu^3}{\epsilon}\right)^{\frac{1}{4}} \tag{4.35}$$

where ν is the kinematic viscosity, and ϵ is the turbulence dissipation rate (Equation 4.36), which depends on the turbulence model chosen. In this case, due to the fact that the flow passes through an open-circuit wind tunnel, there will likely be flow separation in the diffuser. Therefore, the turbulence model must be sensitive to these conditions, which is why the k-ω SST (Shear Stress Transport) model is used. This model is particularly well-suited for flows with adverse pressure gradients and separation, making it ideal for wind tunnel analysis. Since the simulation is in OpenFoam these parameters have to be really understood because if the wrong values are given either the simulation does not run properly or does not converge. In open foam the value of the dissipation rate is calculated based o the turbulent kinetic energy (k) and the the specific dissipation rate (ω), multiplying those two and the model constant (C_μ), typically around 0.09 for the maximum velocity expected of 20 m/s in the test section. And those values are obtained as seen in equations 4.37 and 4.38 respectively.

$$\epsilon = C_\mu k\omega \tag{4.36}$$

$$k = \frac{3}{2} \cdot (U_\infty \cdot I)^2 \tag{4.37}$$

$$\omega = \frac{k^{0,5}}{L} \tag{4.38}$$

Where L is the turbulence length scale which is the longest edge times 0,007 and I is the turbulence intensity. This factor gives the level of turbulence and can be defined as in equation 4.39. Although it can also be estimated based on the Reynolds number (Re) using the equation 4.40. This method is particularly helpful for simulations when experimental data on turbulence intensity isnt available like in this case. By relating intensity to the Reynolds number, it allows

for an estimation that reflects the flow regime. It measures the turbulent intensity at the core of a pipe for a fully developed pipe flow.

$$I = \frac{u'}{U_\infty} \tag{4.39}$$

$$I \approx 0{,}16 \cdot \mathrm{Re}^{-1/8} \tag{4.40}$$

where u' = velocity fluctuations due to turbulence. By compiling these values and taking into account the Reynolds number for each section, as well as a density of 1.184 kg/m^3 and a dynamic viscosity of 1.849 x10^{-5} Kg/m*s for a temperature of 25° C, the tunnel conditions are adjusted to reflect the average temperature in the city of Cali [36].Therefore the information shown in Table 4.3 is obtained. It can be observed that the largest Kolmogorov scale is 0.083 m for all the cases, meaning that the maximum element size in the mesh should not exceed this value.

Table 4.3: Simulation Parameters for Different Velocities

Test Section Velocity [m/s]	**Initial Velocity** [m/s]	**Reynolds** [-]	$\boldsymbol{k}$ $\times 10^{-3}$ [m^2/s^2]	$\boldsymbol{\omega}$ $\times 10^{-3}$ [1/s]	$\boldsymbol{I}$ [%]	$\boldsymbol{\epsilon}$ $\times 10^{-3}$ [m^2/s^3]	$\boldsymbol{v}$ $\times 10^{-3}$ [m^2/s]	$\boldsymbol{\eta}$ $\times 10^{-3}$ [m]
20	2.9585	123140	17.876	2.941	3.692	4.730	6.081	83.012
15	2.2189	92356	10.833	2.293	3.834	2.230	4.743	83.111
10	1.4792	61568	5.330	1.602	4.032	0.767	3.321	83.096
5	0.7396	30784	1.580	0.874	4.395	0.124	1.812	83.110

4.2. Mesh Parameters

Accordingly, three meshes were selected that fulfilled these conditions, and a 4 % mesh independence study was performed using the velocity profile to ensure that the results were not dependent on the mesh size. Set due to the high consistency of experimental data, with an uncertainty of 10^{-6}, and a velocity variation of less than 2.5 %, as shown in the graphs of section 5. Given the low uncertainty and minimal variation. The Root Mean Square Error (RMSE) was used to perform the mesh independence analysis. This is a measurement that quantifies the differences between velocity profiles of successive mesh refinements, and the procedure consists on obtaining the velocity profile for each mesh at the same point and at each point determine the difference between two different meshes and using the equation 4.41 for RMSE and select the mesh that mashes the criteria. The RMSE is justified as the study focuses on velocity profiles. This ensures mesh independence for accurate flow dynamics in the test section. While global criteria like total friction force could be used, RMSE effectively validates velocity distribution, crucial for the simulations reliability.

$$RMSE = \sqrt{\frac{1}{N}\sum_{i=1}^{N}(V_{mesh1,i} - V_{mesh2,i})^2} \tag{4.41}$$

where $V_{\mathrm{mesh1},i}$ and $V_{\mathrm{mesh2},i}$ are the velocity values at point i for Mesh 1 and Mesh 2, respectively, and N is the total number of points. Finally the information of each mesh is located in the table 4.4

Mesh	Nodes	Elements	RMSE
1	132970	300467	-
2	356238	762717	6.64
3	656605	1543234	0.35

Table 4.4: Mesh Independency with RMSE values.

Based on the criteria established, Mesh 2 already offered a reasonable level of precision. This indicated that the mesh was accurate enough to provide reliable data. However, to obtain even more precise and detailed results, Mesh 3 was chosen based on its lower RMSE (0.35) compared to Mesh 2 (6.64). A lower RMSE indicates that the velocity profiles between different mesh refinements are more similar, implying better convergence and fewer numerical discrepancies. Although this meant more computational time, it allowed for capturing finer details in the velocity profile, ensuring that the results were not only consistent but also more accurate. Opting for Mesh 3 helped minimize potential variations and increased the confidence in the simulation outcomes. Having this mesh the parameters mentioned in the last section has to be review, the working mesh has to fulfill the criteria illustrated before. These parameters can be seen in table 4.5where all four values are within the parameters for proper mesh performance.

Table 4.5: Mesh Quality Parameters

Parameter	Value
Max Aspect Ratio	6.622
Max Non-Orthogonality	59.57°
Skewness	0.799
Max Cell Length	0.020 m

As shown in Figure 4.28, the mesh has a refinement along the edges. This refinement helps capture the phenomena occurring in these areas more accurately, as they are critical zones where adverse pressure gradients or layer separations can occur. Therefore, it is essential to mesh these areas with small elements to achieve results that closely resemble real-life behavior. In this case, tetrahedral elements were used for the mesh to better adapt to the sections; however, this is not a key criterion that would affect the results in this type of simulation.

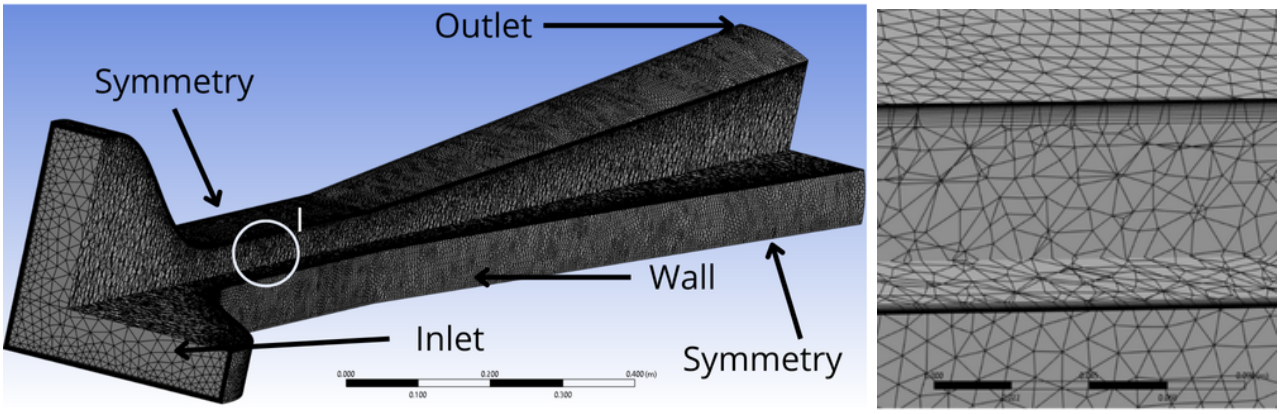

(a) Internal isometric mesh view **(b)** Detail I

Figure 4.28: Working mesh. Source: [Author]

In the figure 4.28b is shown the inflation in the borders. This is important because if this is not made the phenomenon in the surface does not receive the information needed for the turbulent model.Since it represents a quarter of the complete section, symmetry faces, as well as inlet and outlet boundaries and the wall, need to be established so that the software correctly identifies how the flow should behave at these limits. Furthermore, tetrahedral elements were used for the mesh due to their ability to conform more easily to complex geometries, ensuring better adaptability and coverage in areas with irregular shapes.

4.3. OpenFOAM Parameters

Once the mesh was established, boundary conditions were set, and necessary assumptions were made, such as assuming the flow to be incompressible. This assumption is valid because the Mach number is less than 0.3, indicating that compressibility effects are negligible [1]. Specifically, the Mach number in the test section is 0.058, further confirming that the flow remains incompressible. The Mach number (M) is a critical parameter in airflow simulations, helping to determine whether compressibility effects are significant in the flow. It is defined as the ratio of the flow velocity (v) to the speed of sound (a) in the medium as described in the equation 4.42:

$$M = \frac{v}{a} = \frac{v}{\sqrt{\gamma \cdot R \cdot T}} = \frac{20}{\sqrt{1{,}38 \cdot 0{,}286 \cdot 300}} = 0,058 \tag{4.42}$$

The initial simulation started under the assumption of steady-state conditions using the SimpleFoam solver. However, after several attempts, the residuals failed to converge, and upon visual inspection of the simulated model, it was observed that after a certain period, a significant disturbance emerged. This behavior indicated that the assumption of steady-state flow might not have been appropriate.

As a result, it was decided to switch to a transient simulation using the PimpleFoam solver. The change was motivated by the observation of small vortices forming in the corners of the domain. These vortices, when treated under a steady-state assumption, introduced instability and caused the simulation to diverge. By employing a transient simulation, these dynamic flow features were better captured, allowing the residuals to converge and providing results that more accurately represented the expected physical behavior of the system. The parameters used in the simulations are seen in table 4.3

The solver is responsible for modeling turbulent flow using the Reynolds-Averaged Navier-Stokes (RANS) equations (4.43. This approach allows us to observe how the flow behaves in different parts of the tunnel over time, providing a time-averaged view of the turbulence. By averaging out the fluctuations, RANS simplifies the complex, chaotic nature of turbulent flow, making it easier to analyze and predict the overall flow patterns in the wind tunnel.

$$\frac{\partial(\rho U_i)}{\partial t} + \frac{\partial(\rho U_i U_j)}{\partial x_j} = -\frac{\partial P}{\partial x_i} + \frac{\partial}{\partial x_j}\left[\mu\left(\frac{\partial U_i}{\partial x_j} + \frac{\partial U_j}{\partial x_i}\right) - \rho\overline{u_i' u_j'}\right] \tag{4.43}$$

where

- U = mean flow velocity
- u' = velocity fluctuations due to turbulence
- μ = molecular viscosity

- $-\rho u_i' u_j'$ = Reynolds Stress term

The turbulence model used was kω-sst (shear stress tensor) which is solved with RANS. this model is good to represent the behavior of a turbulent flow during a period of time. It offers improved predictions of flow separation compared to most RANS models and demonstrates reliable performance under adverse pressure gradients. Additionally, it effectively accounts for the transport of principal shear stress in boundary layers experiencing adverse pressure gradients.

This is a two-equation model, which, in addition to the fundamental conservation equations, provides a comprehensive description of the flow. The mass conservation equation, as presented in equation 2.1, describes the continuity of mass within the fluid flow. Similarly, the momentum conservation is expressed through equation 4.44, governing the forces acting on the fluid elements. The energy conservation is detailed in equation 4.45, accounting for the energy transformations within the system. Furthermore, the model includes the turbulent kinetic energy (k) equation, represented in equation 4.46, and the specific turbulent dissipation rate (ω), which is defined in equation 4.47. These additional equations allow for the modeling of turbulence, making the model more robust for analyzing complex fluid behavior.

$$\frac{\partial(\rho U_i)}{\partial t} + \frac{\partial(\rho U_i U_j)}{\partial x_j} = -\frac{\partial P}{\partial x_i} + \frac{\partial}{\partial x_j}\left[\mu\left(\frac{\partial U_i}{\partial x_j} + \frac{\partial U_j}{\partial x_i}\right)\right] + \frac{\partial}{\partial x_j}\left(-\rho u_i' u_j'\right) \tag{4.44}$$

- U_i : Velocity components
- P : Pressure
- μ : Molecular viscosity
- $-\rho u_i' u_j'$: Reynolds stress term

$$\frac{\partial(\rho E)}{\partial t} + \frac{\partial(\rho U_j E)}{\partial x_j} = \frac{\partial}{\partial x_j}\left(k_{eff}\frac{\partial T}{\partial x_j}\right) + \mu_{eff}\Phi - \frac{\partial q_j}{\partial x_j} \tag{4.45}$$

- E : Total energy
- k_{eff} : Effective thermal conductivity
- T : Temperature
- $\mu_{eff}\Phi$: Viscous dissipation
- q_j : Heat flux

$$\frac{\partial(\rho k)}{\partial t} + \frac{\partial(\rho k U_j)}{\partial x_j} = P_k - \beta^* \rho k \omega + \frac{\partial}{\partial x_j}\left[\left(\mu + \frac{\mu_t}{\sigma_k}\right)\frac{\partial k}{\partial x_j}\right] \tag{4.46}$$

- P_k : Production of turbulent kinetic energy
- β^* : Model constant
- μ_t : Turbulent viscosity

- σ_k : Prandtl number for k

$$\frac{\partial(\rho\omega)}{\partial t} + \frac{\partial(\rho\omega U_j)}{\partial x_j} = \alpha\frac{\omega}{k}P_k - \beta\rho\omega^2 + \frac{\partial}{\partial x_j}\left[\left(\mu + \frac{\mu_t}{\sigma_\omega}\right)\frac{\partial\omega}{\partial x_j}\right] + 2(1-F_1)\frac{\rho\sigma_{\omega 2}}{\omega}\frac{\partial k}{\partial x_j}\frac{\partial\omega}{\partial x_j} \quad (4.47)$$

- α : Model constant for ω
- β : Model constant
- F_1 : Blending function in the SST model
- $\sigma_{\omega 2}$: Prandtl number for ω

In OpenFOAM, the folders containing the parameters for the previously mentioned equations must be set up in advance. Specifically, folders for velocity, pressure, and, for this case, the parameters for k and ω as well as for kinematic viscosity (v) need to be defined.The website called FluidsMechanics101 helps finding the parameters required for the simulations in OpenFoam [37]. In these folders, it is essential to correctly establish the turbulence model and kinematic viscosity, and it is especially important to clearly define the geometry faces and denote the boundary conditions. In this case, as shown in Figure 4.28, four sections were denoted: inlet, outlet, wall, and symmetry, so that the program knows how to behave when interacting with these faces.

An initial velocity must be defined at the wind tunnel inlet according to the desired velocity in the test section, and these values can be seen in Table 4.3. Finally, to start the simulation, the ControlDict file needs to be edited to set the simulation time; this is crucial to maintain a low Courant number. The maximum Courant number reached in the simulation was 5.4, which is important because it affects numerical stability. A high Courant number can lead to instability, making it harder for the simulation to converge and potentially introducing numerical errors.

The simulation is then allowed to run until the final time comes up and the residual values reach the desired level. In this case, a Δ T of 0.00001 seconds was set for a final time of 15 seconds, and each simulation was left running for several hours; the speed at which it completes depends on the computing power available. The boundary conditions and parameters can be found in Table 4.6.

Table 4.6: Boundary Conditions and Model Parameters

Boundary Condition	
Condition	**Parameter**
Inlet	Velocity inlet = 2.958 m/s
Outlet	Pressure Outlet = 0
Wall	No-slip and Adiabatic condition
Symmetry	Symmetry plane
Model and Grid Parameters	
Parameter	**Value**
Flow regime	3-D, Transient
Turbulence model	k-omega SST
Grid type	Tetrahedrals
Number of grid elements	1543234
Convergence time	0.204 seconds

4.4. y+ parameter

Once the simulation is complete, it is important to carefully examine the results, looking at the shape and contours to see if they behave as expected or if adjustments are needed. One critical factor to check is y^+. This parameter is a dimensionless value in computational fluid dynamics (CFD) that measures how close the center of the first cell is to the wall. Its defined as seen in equation 4.48. where y is the distance from the wall to the cell center, u_τ is the friction velocity and ν the cynematic viscosity.

$$y^+ = \frac{y u_\tau}{\nu} \tag{4.48}$$

This parameter is critically important because, depending on the turbulence model used, it indicates whether the simulation will accurately describe the phenomenon. y^+ reflects how well the boundary layer behavior is captured. For kω-SST the closer this value is to 1, the more accurately the simulation can represent the boundary layer dynamics.

In Figure 4.29, the y^+ values are shown for the case of 20 m/s velocity in the test section. The contour map illustrates the y^+ distribution across the section, highlighting how effectively the boundary layer is captured at this speed. As shown in the image, the highest y^+ values are found along the walls, which is expected due to the increased flow complexity in these areas. At the walls, factors such as pressure gradients and changes in flow direction lead to higher friction velocities, which in turn result in elevated y^+ values. This pattern is consistent with boundary layer dynamics, where wall boundaries experience more frictional forces that influence y^+ behavior.

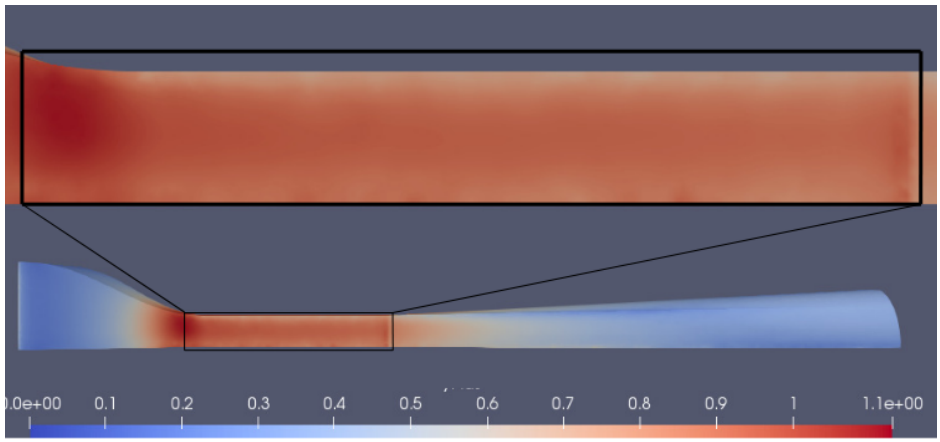

Figure 4.29: Y+ wall Contour at 20 m/s. Source: [Author]

In Table 4.7, the y^+ values for each target velocity in the test section are presented. These values are crucial for validating whether the mesh near the walls meets the criteria for accurate flow simulation, confirming that the simulation has captured an appropriate level of detail within the boundary layer. Given that for the k-ω SST model, this y^+ value should ideally be below 1, the table provides insight into the adequacy of the mesh for this turbulence model.

Table 4.7: Mean and Maximum y^+ values at different velocities in the test section

Velocity in Test Section [m/s]	**Mean y^+**	**Max y^+**
20	0.487	1.171
15	0.385	0.908
10	0.278	0.637
5	0.142	0.353

In this simulation, the y^+ maximum value seen in table 4.7 is founs at 20 m/S and is 1.171, which aligns well with the ideal target for the $k-\omega$-SST turbulence model when aiming to resolve the boundary layer in detail. This low y^+ value signifies that the mesh near the wall is fine enough to capture the viscous sub-layer accurately, allowing for a high level of precision in modeling near-wall phenomena without the need for wall functions. Achieving $y^+ < 1$ enhances the reliability of the simulation, as it ensures that the boundary layer's detailed behavior, including the friction and pressure gradients close to the wall, is fully resolved. This level of detail is particularly beneficial for studies focusing on flow separation, adverse pressure gradients, and other critical near-wall effects.

5. Data recompilation

In this chapter, the methodology and process used to gather velocity profile data are presented, covering both simulation with OpenFOAM and experimental measurements using a static Pitot tube in the wind tunnel. The design and construction of an attachment that enables experimental data collection are discussed, explaining how this setup allows for accurate measurements. Additionally, the method for obtaining turbulence intensity experimentally is shown, followed by a comparison with values estimated through theoretical calculations. Finally, a comparison between both cases is made, and the results are illustrated to highlight the findings.

5.1. Experimental results

The experimental data was collected using a static Pitot tube and a differential pressure sensorarregment seen in figure 5.30 to measure the differential pressure between the static and stagnation pressure, thereby obtaining the dynamic pressure.

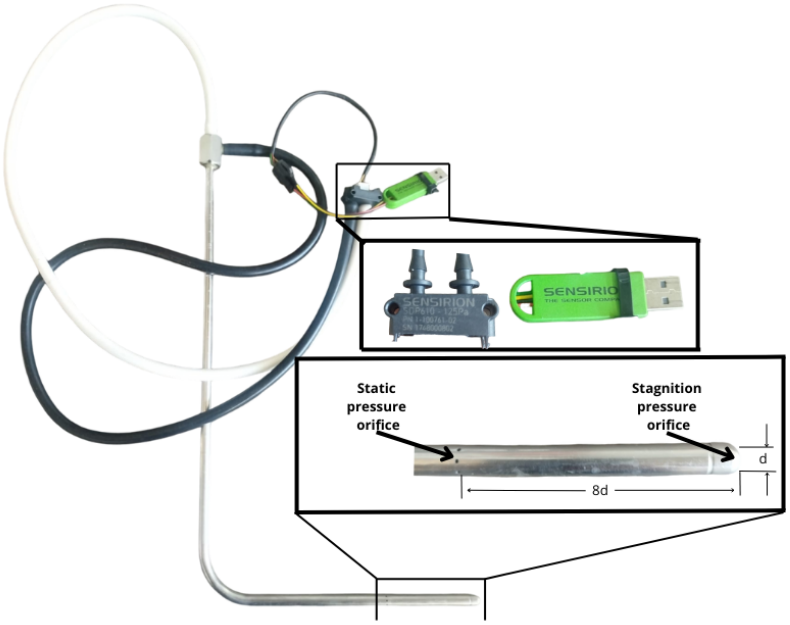

Figure 5.30: Pitot static tube. Source: [Author]

This fluid mechanics tool helps determining the pressure difference at a specific point by measuring the stagnation pressure and the static pressure. Using differential pressure sensors, the dynamic pressure is obtained, as shown in Equation 2.4. With this equation, data processing is

then performed to calculate the velocity at that point. This measurement was carried out in the central plane of the test section of the wind tunnel, following a grid of points spaced 2 cm apart both horizontally and vertically, covering the entire plane. The data collection process employed Sensirion pressure SDP 6X Series sensors seen en figure 5.30 that were connected to de computer by an USB port. There were three sensors for different ranges, up to 25, 125 and 500 Pa, with an uncertainty of 0.001 Pa, ensuring high precision in the pressure readings.

To achieve this, an setup was designed to position and hold the static Pitot tube in the desired location, as shown in Figure 5.31. A piece was created to be fixed to the lateral side of the test section structure, securely holding the Pitot tube and allowing it to be adjusted according to the required measurement distance. As explained in the test section design, this setup allows for cross-sectional measurements without pressure loss.

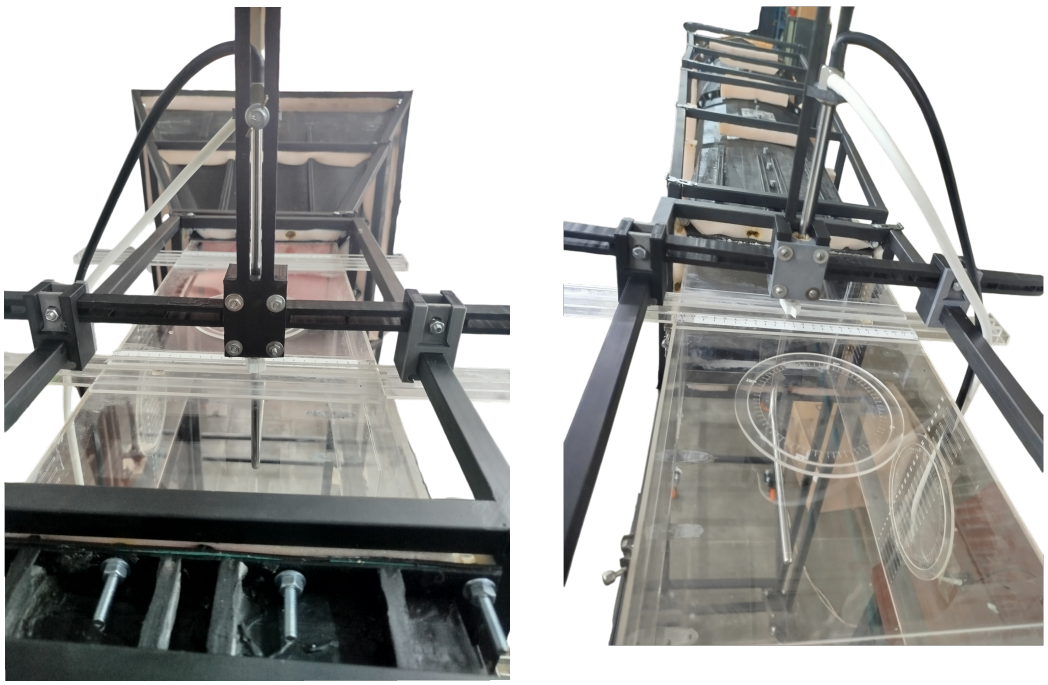

(a) Rear view **(b)** Frontal view

Figure 5.31: Experimental measurements setup. Source: [Author]

The first step was to characterize the fan's Revolutions Per Minute (RPM) to determine the RPM needed to achieve a certain velocity. This was done using a tachometer. A piece of reflective tape was placed on one of the fan blades, and the tachometer detected the frequency with which this tape appeared using a laser, thereby obtaining the RPM. The setup was calibrated by setting a specific speed in the wind tunnel and measuring the pressure at the center of the test section. Using Equation 2.4, the pressure value was substituted to determine the actual speed. When the desired speed was reached, it was kept constant and recorded. In this way, the RPMs were characterized, as shown in Table 5.8.

Table 5.8: RPM Values for Different Desired Velocities

Velocity [m/s]	RPM
23.5	1470
20	1268
15	995
10	665
5	350

By examining the revolutions at maximum speed and referencing the fan information in Section 3.2, which states that the fan's maximum RPM is 1470, it is clear that the actual maximum speed is not 20 m/s. When measured, this maximum speed reaches 23.5 m/s. However, to facilitate a gradual analysis of velocity values, an analysis at 20 m/s was chosen.

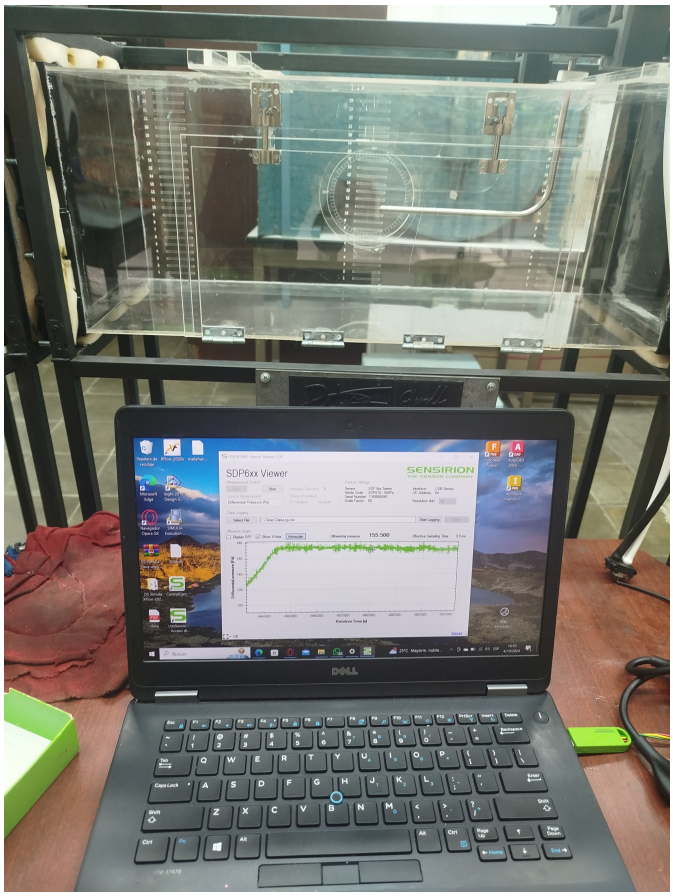

Figure 5.32: Experimental Setup. Source: [Author]

For each measurement position, data was recorded with a sampling frequency of 9 microseconds over a 20-second period. After completing the data acquisition at each point, the average of the recorded values was calculated and assigned to the corresponding location on the plane. This averaging reduces data fluctuations, ensuring that the measurements are more representative of the actual flow behavior. Subsequently, the dynamic pressure equation (second term in equation 2.4)was used to calculate the flow velocity at each point of the measurement grid. It is important to account for uncertainty propagation in this analysis, as the position measurements were taken

with a ruler, introducing a position uncertainty. Additionally, the pressure readings come with the before mentioned uncertainty of 0.001 Pa, which should be considered when calculating the final velocity. The accuracy of the sensors and the stability of the flow help minimize the impact of these uncertainties, but their effect must be quantified.

This process was held for each velocity 20 m/s, 15 m/s, 10 m/s and 5 m/s in order to characterize more that just one velocity plane. In figure 5.33a can be seen the movement in Y direction and in figure 5.33b can be seen the movement in Z direction. Also, there is a ruler drawn because the real ruler is graved in the acrylic and is not appreciated in the picture. Besides, The velocity plane can be seen and it is located at half the total test section length.

Once the velocities were obtained at all points of the grid, 2D graphs were constructed to represent the velocities in each column and row of the measurement plane. Subsequently, the velocities were interconnected to generate a 3D graph of the plane, representing the velocity profile in the test section. This visualization allows for evaluating the flow distribution and the symmetry of the velocity profile along the wind tunnel and is later compared to the results obtained in the simulations.

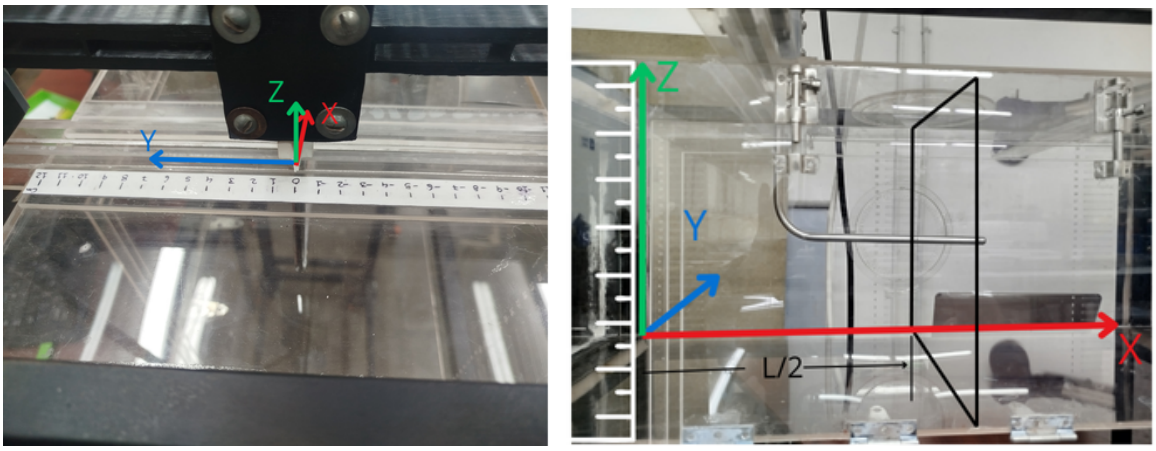

(a) Movement in x direction **(b)** Movement in Z direction

Figure 5.33: Differential pressure measurements procedure. Source: [Author]

After completing the scan every 2 cm in the Y and Z directions, data was collected at a total of 121 points on the plane shown in Figure 5.33b for each of the 4 velocities. For each point, measurements were taken to capture the relevant information.

To measure the velocity plane, the static pitot tube was used to measure the pressure every 2 cm in the Y and Z directions in the central plane of the test section in figure 5.33b, as previously mentioned, to collect velocity information in a total of 121 point for each of the 4 velocities. the pressure sensor measures with a sampling frequency of 0.009 seconds. Each point was measured during approximately 20 second giving a total of 2222 measures per point. All measurements were conducted without any data processing. The data collection alone took approximately one week to ensure effective data acquisition.

After obtaining all the data, the pressure sensor program saved the readings in spreadsheet files, which included relative time, sample number, and differential pressure. An excerpt of the data from the 12 cm x 12 cm point is shown in Table 5.9. For each of these files, the average value of all measurements was calculated to establish this as the actual value for that point. To validate this value, the standard deviation for each data group was also calculated. This determined whether the data collection accurately represented the real conditions at the point. In all cases,

the standard deviation did not exceed 3 %, indicating that the average of the collected data could indeed be considered as the dynamic pressure value at the measurement point.

Table 5.9: Sample Data of Experimental Differential Pressure at Point 12x12

Sample #	Relative Time [s]	Differential Pressure [Pa]
810619	6783.84	236.350
810620	6783.85	240.400
810621	6783.86	235.883
810622	6783.86	236.350
810623	6783.87	238.467
810624	6783.88	236.533
810625	6783.89	239.583
810626	6783.90	233.783
⋮	⋮	⋮

The differential pressure value for each point was then extracted, and using Equation 2.4, the velocity at each point was calculated. These values were arranged on the plane, resulting in an experimental velocity map at the midpoint of the test section in the wind tunnel. This map is shown in Figure 5.34.

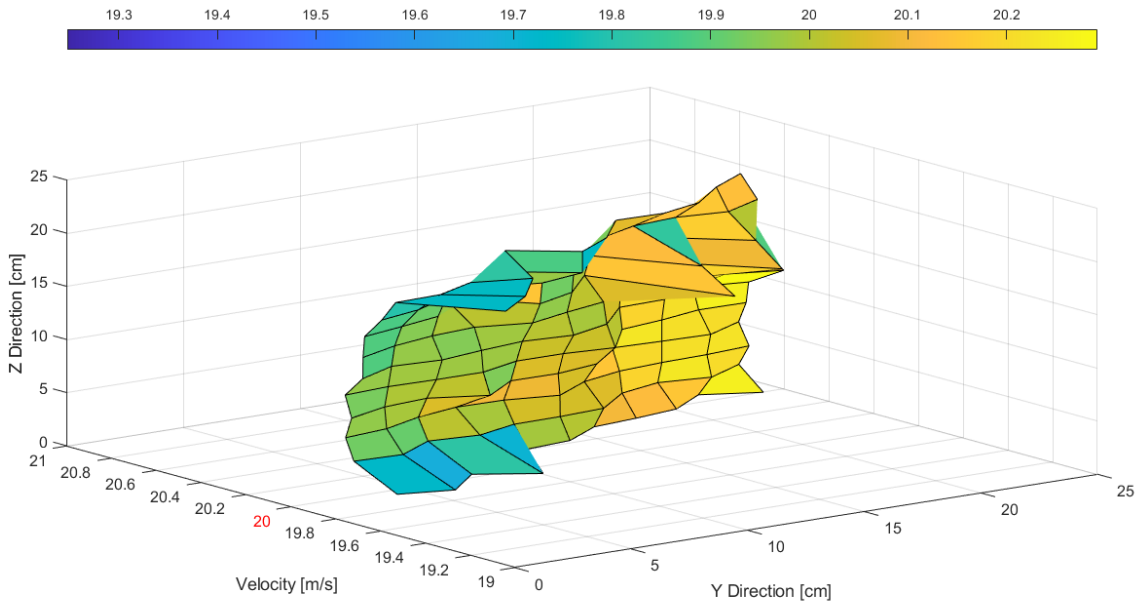

Figure 5.34: Velocity plane in the center of the test section. Source: [Author]

In Figure 5.34, peaks caused by either pressure gradients, turbulence or flow separation, or non-uniform inlet flow can be observed mainly along the edges. But given the velocity range of 19-20 m/s, it is clear that the data tends to converge towards 20 m/s, showing minimal errors. In fact, this range was chosen for the graph to make the differences more visible; otherwise, the profile would appear completely flat. In Table 5.10, the information on the maximum and average

percentage errors for each data measurement is compiled relative to its expected value (5, 10, 15 and 20 m/s).

Table 5.10: Maximum and Average Percentage Errors for Each Experimental Velocity

Expected Velocity [m/s]	**Max Percentage Error [%]**	**Average Percentage Error [%]**
20	3.76	0.68
15	3.53	0.62
10	3.61	0.64
5	2.86	0.77

The analysis of the maximum and average percentage errors for each expected velocity shows that the experimental data closely align with the target values (20 m/s, 15 m/s, 10 m/s, and 5 m/s). The maximum errors remain low, with a peak of 3.76 % and an average under 1 %, indicating high accuracy in data collection and stable flow within the wind tunnel's test section. This low error level suggests that the experimental conditions were well-suited to capturing the expected flow behavior, making the data reliable and representative for further analysis and simulations.

5.1.1. Turbulent Intensity

The turbulence intensity provides the level of turbulence and can be defined as shown in equation 4.39. This level of turbulence is crucial to assess the quality of the flow, and in subsonic wind tunnels, it is expected to remain low to ensure the reliability of experiments conducted in the tunnel. Therefore, it is important to determine this value accurately.[1]

The same set of data from the velocity case is taken to find this parameter. In turbulence analysis, it is crucial to obtain a good representation of fluctuations, which is achieved with a sufficient number of samples. The 2222 measurements were reduced to 500, maintaining 25 samples/s, sufficient to capture pressure variations if the signal is stable to capture the characteristic temporal scales of the flow in the wind tunnel. Controlled downsampling preserved information without bias or significant loss. It is enough to ensured that several typical fluctuations of the turbulent flow are captured, allowing for precise characterization of both the intensity and the nature of the turbulence. This number of data points provides a balance between statistical representativeness and temporal efficiency, while avoiding the collection of an excessive number of samples that would not contribute additional significant information and would require more computational resources.

With the help of a MATLAB code, the pressure data at each point was converted to velocity using Equation 2.4, and the turbulence intensity was calculated using Equation 4.39. This process took time as the temporal data was entered for each position in the matrix. Finally, Figure 5.35 shows the experimental turbulence intensity at the mid-plane of the test section at 20 m/s.

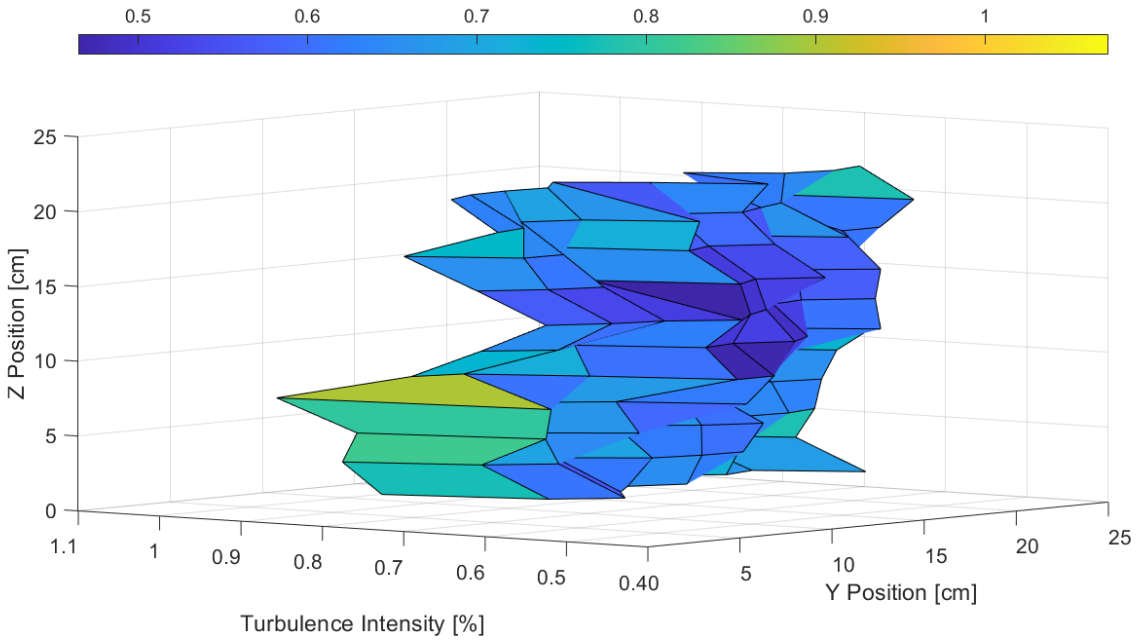

Figure 5.35: Experimental turbulence intensity at 20 m/s in the test section. Source[Author]

In the figure, the values at each point on this plane can be observed, showing that the behavior at each velocity remains stable. The areas with the most significant fluctuations are located in the corners, which makes sense, as the flow can exhibit greater fluctuations at these points as seen in the velocity plane. The maximum, average values for the four velocities are provided in Table 5.11 along with the percentage difference between the experimental turbulence intensity and the calculated using equation 4.40 for the simulations.

Table 5.11: Experimental Turbulence Intensity Values for Different Speeds

Velocity [m/s]	I_{exp} **Mean [%]**	I_{exp} **Max [%]**	**Percentage Difference[%]**
20	0.64	1.07	82.67
15	0.64	1.13	83.61
10	0.68	1.83	83.13
5	1.41	2.34	67.92

It is observed that as the velocity decreases, the turbulence intensity value increases. This result aligns with Equation 4.39, where turbulence intensity is defined as the ratio between the flow fluctuation and the mean value. Therefore, as the flow speed decreases, any disturbance has a greater impact on this measurement. This means that as the velocity inside the wind tunnel is lower, the tunnel becomes more unstable.The percentage errors between the measurements are mainly due to the fact that they were calculated using different methods. One method relied on the Reynolds number and did not account for the real fluctuations of the phenomenon, as these fluctuations were not fully understood at the time. In contrast, the other method did use these real fluctuations, providing a clearer picture of the actual phenomenon. Therefore, the experimental value is the closest approximation and better reflects the true behavior of the flow.

5.1.2. Experimental Pressure Losses

The pressure losses identified in each section of the wind tunnel were measured by static pressure at specific points within the tunnel, which was then used to determine the pressure losses in each section. Due to the fan being directly coupled to the diffuser, the pressure measurement at the diffusers exit was taken 30 cm before the end of the section to avoid any interference from the fan. The measurement procedure involved blocking the stagnation pressure port of the Static Pitot Tube to obtain only the static pressure, ensuring accurate readings for each section. The wind tunnel is equipped with multiple orifices along its length, specifically designed to allow pressure measurements at various points.

For each measurement, the Pitot tube was inserted into these orifices, and the static pressure values were recorded. However, for this experiment, a differential pressure sensor was not used, as it was unable to perform the required readings. Instead, a manometer was connected to the Pitot tube to capture the pressure values. This process included measuring pressure losses in sections such as the honeycomb, test section, contraction zone, and diffuser.

In Table 5.12, the experimentally gathered data on these pressure losses are presented.

Table 5.12: Pressure losses in wind tunnel

Section	$\Delta P_{Losses}[Pa]$
Test Section	1.406
Honey Comb	6.392
Contraction Zone	232.620
Diffuser	113.856

This experimental data serves as a foundational reference for evaluating the tunnels performance and will later be compared with simulation results.

5.2. Simulation results

The data acquisition process for the simulation is the same as for the experimental setup, but in this case, there is more information available, so the information had to be filter out what is unnecessary. The first step is to make a cut along the plane in the middle of the test section of the wind tunnel and collect velocity information directly without using pressure, as the simulation already provides velocity data as illustrated in figure 5.36

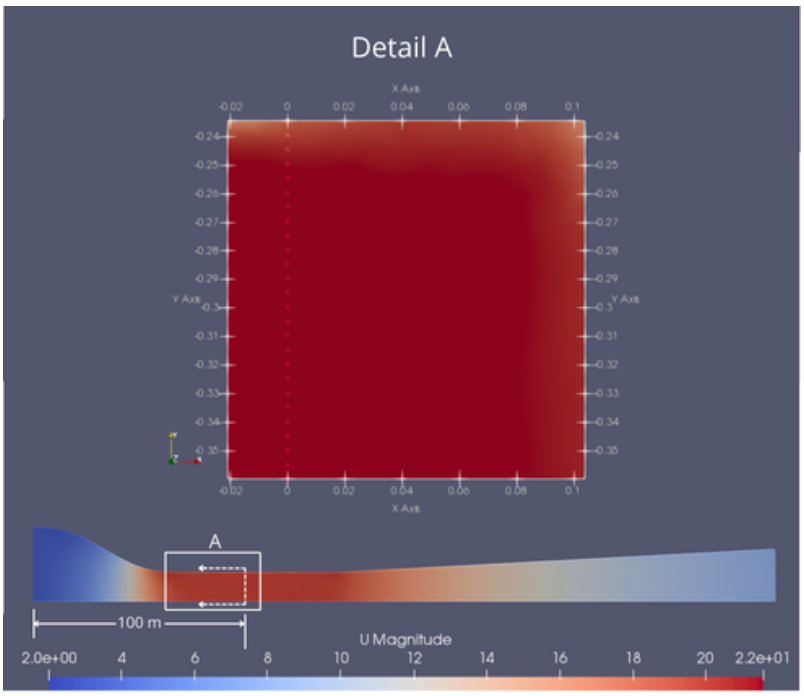

Figure 5.36: Test section mid plane in simulation: [Author]

A line is then created on the surface that passes through the same points where experimental data was taken, moving this line 2 cm to the right each time. Since the data was recorded every 2 cm and the section measures 25 cm along the edge, the middle does not align perfectly with a profile where measurements were taken. Therefore, the line that collects the information must be positioned to capture data on both sides by using symmetry. An insigth of one row of points evaluated as described before can be seen in figure 5.37.

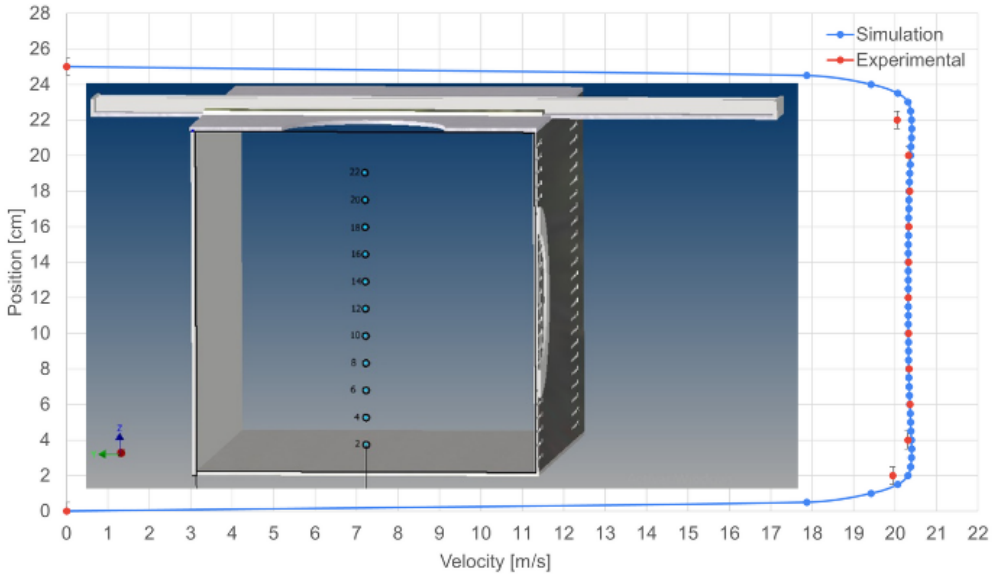

Figure 5.37: Simulation data recompilation. Source: [Author]

Once the data is collected, the corresponding data from the opposite side of the symmetry is

also taken, providing a complete set of data points. The values are then discretized to match the specific points where experimental values were recorded, as the simulation provides continuous data across the entire plane. Figure 5.37 shows the velocity profile obtained at the distance $y = 12\,\text{cm}$ and indicates the location where the measurements were taken.

In the figure 5.37 It is possible to see the velocity profile at 12 cm from the side of the test section, and thanks to the simulation data, it is evident how the velocity profile separates from the boundary layer.Just as with the experimental data, these profiles need to be created across the entire plane to obtain a comprehensive dataset for comparison. By doing that the velocity plane seen in figure 5.38.

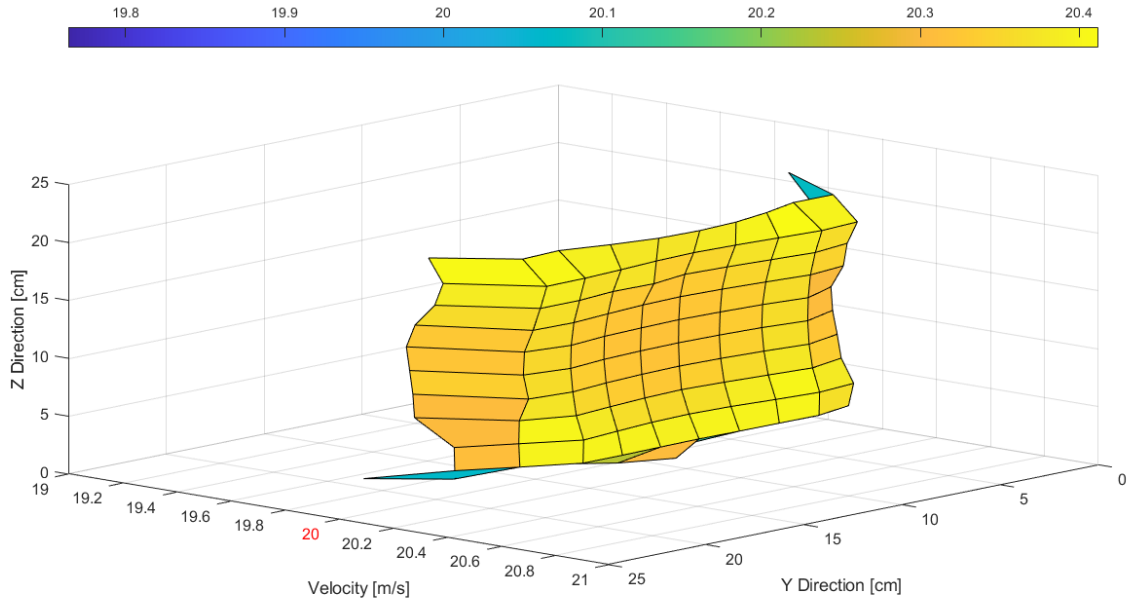

Figure 5.38: Velocity plane in the center of the test section based on simulation. Source: [Author]

In figure 5.38, a profile even more consistent than the experimental data can be seen. This is due to the controlled conditions of the simulation, which reduce external agents that could disturb the flow, as it operates under ideal conditions. In Table 5.13, the information on the maximum and average percentage errors for each data simulated is compiled relative to its expected value (20 m/s, 15 m/s, 10 m/s, and 5 m/s).

Table 5.13: Maximum and Average Percentage Errors for Each Simulated Velocity

Expected Velocity [m/s]	**Max Percentage Error [%]**	**Average Percentage Error [%]**
20	2.06	1.45
15	1.43	1.09
10	1.42	1.01
5	1.44	1.09

The analysis of the maximum and average percentage errors for each expected velocity shows

that the experimental data closely align with the target values (20 m/s, 15 m/s, 10 m/s, and 5 m/s). The maximum errors remain low, with a peak of 3.76 % and an average under 1 %, indicating high accuracy in data collection and stable flow within the wind tunnel's test section. This low error level suggests that the experimental conditions were well-suited to capturing the expected flow behavior, making the data reliable and representative for further analysis and simulations.

5.2.1. Pressure losses in simulation

To determine the pressures along the wind tunnel, pressure results were plotted along the entire symmetry axis, taking into account the points where section changes occurred. The data was downloaded and used to make comparisons between the theoretical and experimental values.

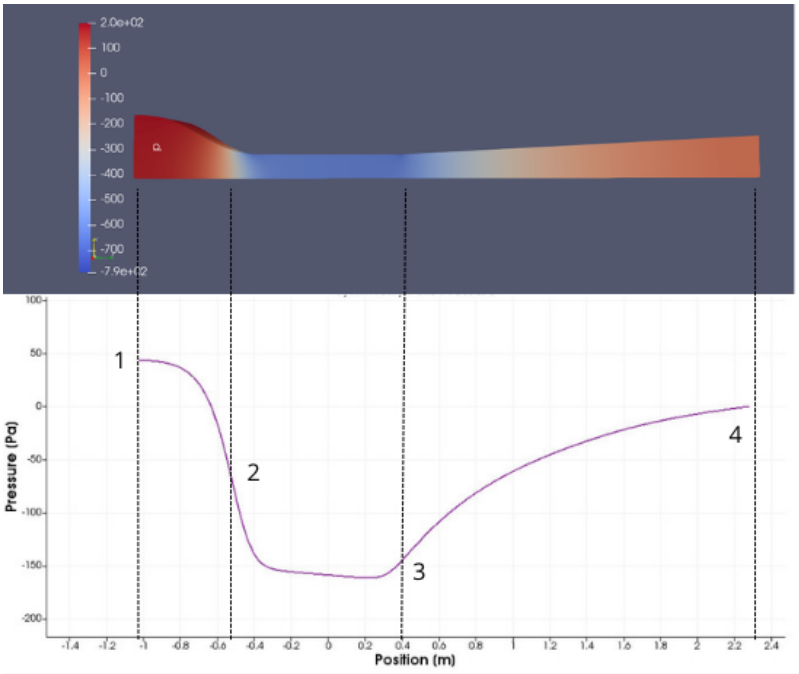

Figure 5.39: Pressure along symmetry axis. Source: [Author]

In the table 5.14 are the values for the pressures measured in the three first places from figure 5.39 since the pressure in 4 is 0 because that is one of the simulation conditions.

Table 5.14: Pressure Along Symmetry Axis Collected

Velocity [m/s]	**Pressure [Pa]**		
	1	**2**	**3**
20	43.276	-145.377	-157.164
15	24.054	-81.022	-88.352
10	11.975	-35.647	-38.852
5	3.277	-8.661	-9.516

Since pressure data was obtained for all zones, by using Bernoullis equation (equation 2.3) with an additional term for losses, the pressure losses could be determined in the simulation. This calculation was performed for four different test section velocities, yielding pressure losses of 10.124 Pa, 5.649 Pa, 2.414 Pa, and 1.356 Pa for velocities of 20, 15, 10, and 5 m/s, respectively.

5.3. Uncertainty Analysis

It is important to perform uncertainty analysis because a scientific method is being applied in which tools with limited resolution are used, and this can cause errors that propagate when one value is used to obtain another. For this reason, uncertainty analysis must be conducted. The first step is to identify the measurements being taken and the instruments used for these measurements; this way, we have the uncertainty of each measurement and can proceed with propagation.

In this case, two measuring instruments were used experimentally: the static Pitot tube and a ruler. As mentioned previously, the Pitot tube has an uncertainty (σ_{Pd})of 0.001 Pa, and the ruler has an uncertainty (σ_L)of 0.001 m. For each particular case, the equation should be used to find the uncertainty of the required value, given by 5.49 for a function $f(x_1, x_2, \ldots, x_n)$, which depends on several variables x_i with associated uncertainties σ_{x_i}.

$$\sigma_f = \sqrt{\left(\frac{\partial f}{\partial x_1}\sigma_{x_1}\right)^2 + \left(\frac{\partial f}{\partial x_2}\sigma_{x_2}\right)^2 + \cdots + \left(\frac{\partial f}{\partial x_n}\sigma_{x_n}\right)^2} \tag{5.49}$$

Where σ_f is the combined uncertainty in the variable f, and σ_{x_i} is the uncertainty in the variable x_i. This equation assumes that the variables x_i are independent and that the uncertainties σ_{x_i} are small relative to the values of x_i.

5.3.1. Velocity uncertainty analysis

For velocity uncerity (σ_u), the equation used is given by 2.4. Solving for u in terms of pressure yields the following equation.

$$\sigma_u = \sqrt{\left(\frac{\partial U}{\partial p_d}\sigma_{p_d}\right)^2} = \left|\frac{\partial U}{\partial p_d}\right|\sigma_{p_d} = \frac{1}{2}\sqrt{\frac{2}{\rho\, p_d}}\,\sigma_{p_d} \tag{5.50}$$

Given that the working density is 1.184 kg/m^3 and the pressure uncertainty is 0.001 Pa and having P_d as the pressure at the evaluated point, the equation 5.51 is used to determine the final uncertainty for the velocity measurement.

$$\sigma_u = \frac{0{,}0006498440561}{\sqrt{P_d}}[m/s] \tag{5.51}$$

5.3.2. Turbulence Intensity uncertainty analysis

Taking into account that the turbulence intensity is experimentally obtained using equation 4.39, where the numerator is the standard deviation of the collected velocity data and the denominator is their mean value, whose uncertainties are $\sigma_{u'}$ and σ_{u_∞} respectively. It is necessary to calculate the uncertainty of these two values, which depend on the velocity. However, in these equations, n refers to the total number of data points (500 as previously stated), and the uncertainty is calculated differently since the value depends on many others. For the standard deviation, the formula used is based on the standard deviation distribution for finite samples as seen in equation 5.52 and for the mean velocity value the equation is equation 5.53.

$$\sigma_{u'} = \frac{\sigma_u}{\sqrt{2(n-1)}} = \frac{\sigma_u}{31{,}591} \tag{5.52}$$

$$\sigma_{u_\infty} = \frac{\sigma_u}{\sqrt{n}} = \frac{\sigma_u}{22{,}361}[m/s] \tag{5.53}$$

Uncertainty is calculated in this way for datasets with a large number of values. Equation 5.52 is derived from the standard deviation distribution for finite samples and from how uncertainties propagate when calculating the standard deviation of multiple measurements. This equation originates from basic statistics, specifically the standard error of the mean. The square root of the number of observations in the denominator reflects how the average of multiple measurements reduces random error [38]. Having these two uncertainties values, the equation 5.49 for the turbulence intensity becomes as seen in equation 5.54

$$\sigma_I = \sqrt{\left(\frac{\partial I}{\partial v'}\sigma_{v'}\right)^2 + \left(\frac{\partial I}{\partial v_\infty}\sigma_{UV_\infty}\right)^2} = \sigma_I = \frac{1}{V_\infty}\sqrt{\sigma_{v'}^2 + \frac{v'^2\sigma_{V_\infty}^2}{V_\infty^2}} \tag{5.54}$$

5.4. Analysis of Results

The velocity planes at the center of the test section were characterized for speeds of 5, 10, 15, and 20, and the comparison of these velocity planes is illustrated in Figures 5.40, 5.41, 5.42, and 5.43. These figures show the behavior of the velocity profile in this plane. It is important to emphasize the range chosen for the axes, as a small range was selected to make even the smallest irregularities visible.

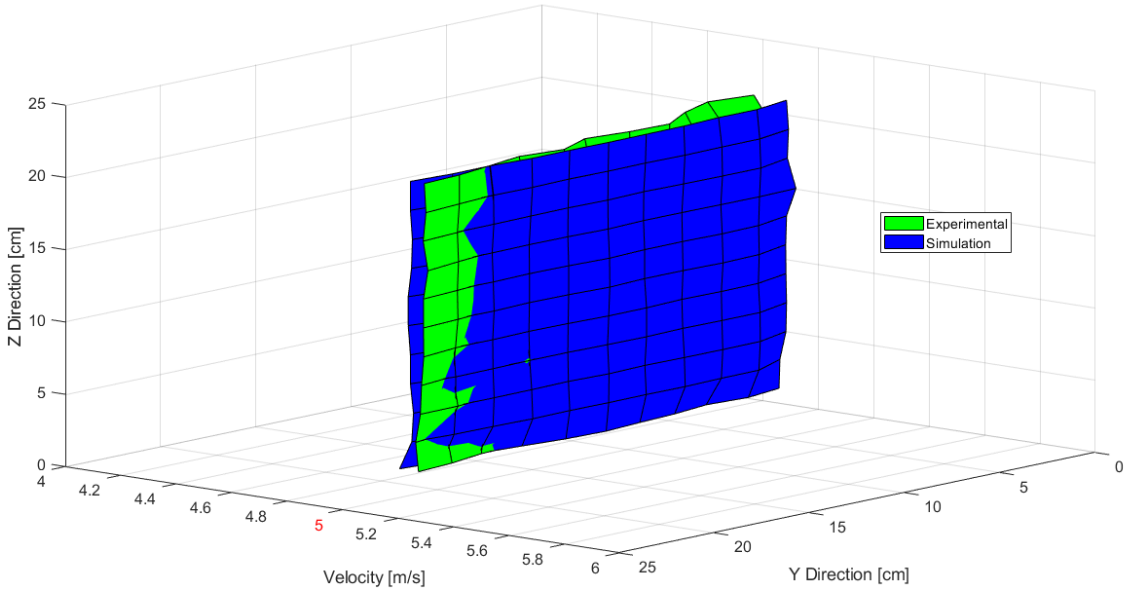

Figure 5.40: Velocities planes comparation at 5 m/s. Source: [Author]

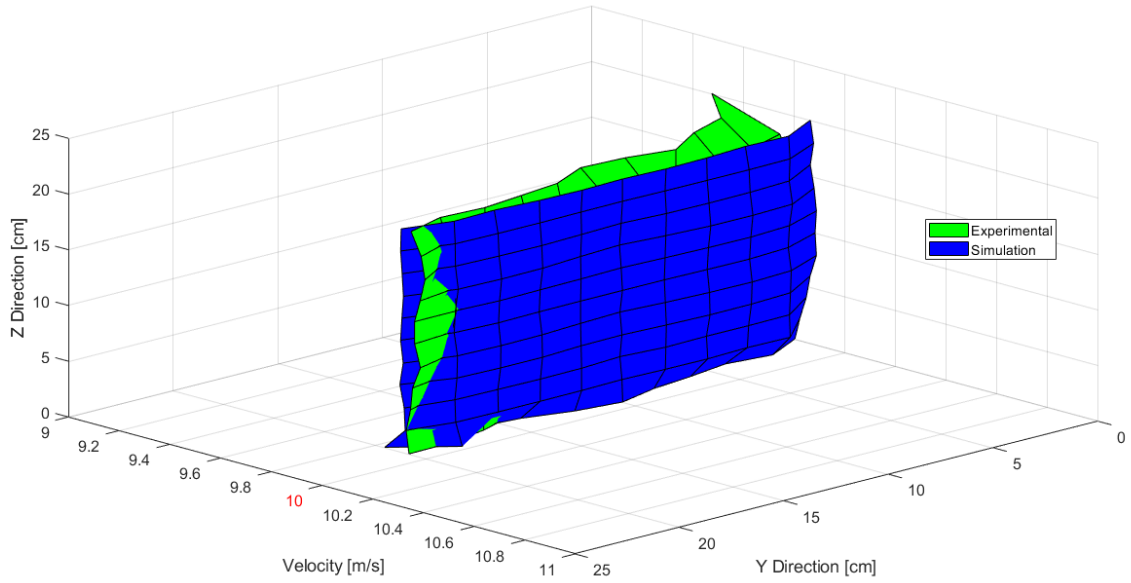

Figure 5.41: Velocities planes comparation at 10 m/s. Source: [Author]

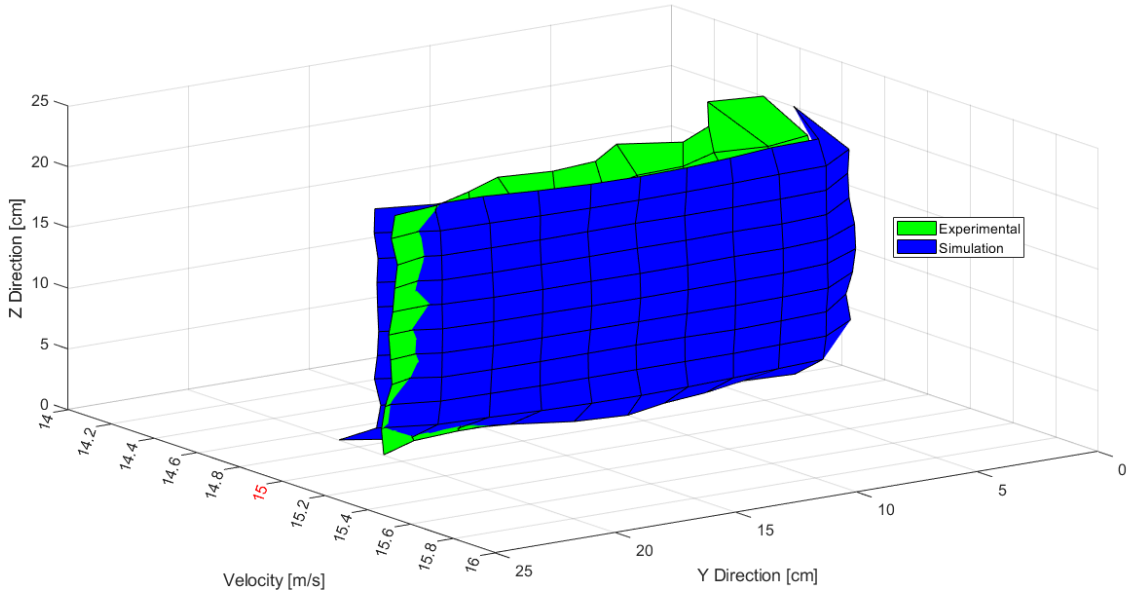

Figure 5.42: Velocities planes comparation at 15 m/s. Source: [Author]

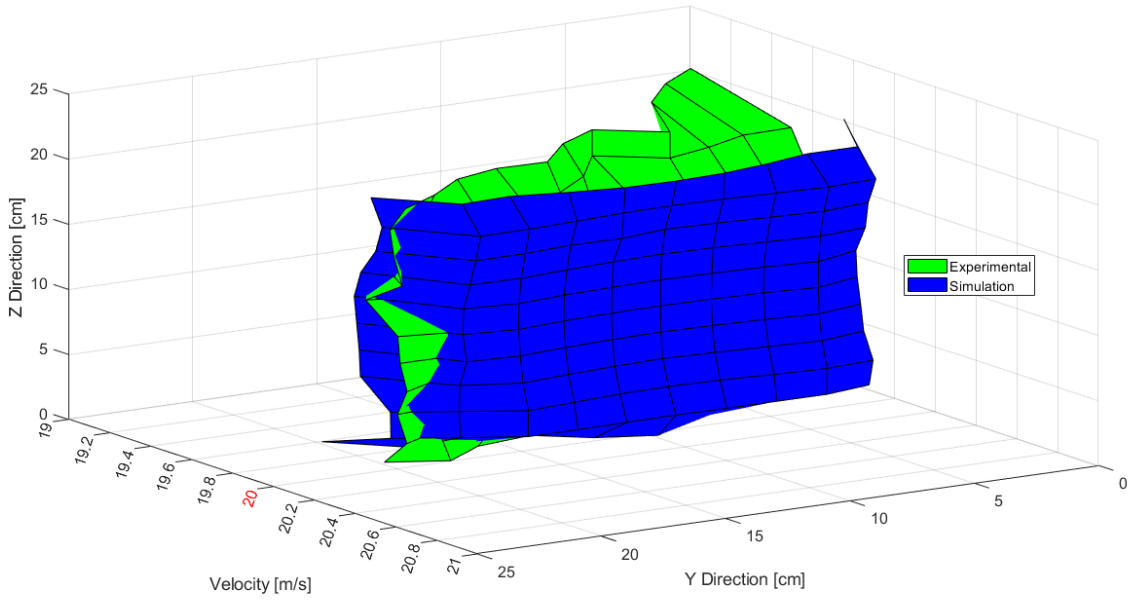

Figure 5.43: Velocities planes comparation at 20 m/S. Source: [Author]

Table 5.15 presents a comparison of the maximum, minimum, and mean velocity values observed in the experimental and simulated data across the four test velocities. Additionally in table 5.16, there is included the absolute error and percentage error for each velocity level, highlighting the differences between experimental and simulated results. This table serves to provide a comprehensive view of the accuracy and precision of the simulation relative to the experimental measurements, allowing for an assessment of model fidelity and insights into any deviations at different speeds.

Experimental Velocity			
Velocity in Test Section [m/s]	**Max [m/s]**	**Min [m/s]**	**Mean [m/s]**
20	20.29	19.25	20.02
15	15.20	14.47	15.00
10	10.16	9.64	10.01
5	5.10	4.86	5.02
Simulated Velocity			
Velocity in Test Section [m/s]	**Max [m/s]**	**Min [m/s]**	**Mean [m/s]**
20	20.41	19.76	20.28
15	15.21	14.80	15.16
10	10.14	9.97	10.10
5	5.07	5.00	5.05

Table 5.15: Experimental and simulated velocity values for different velocities.

Absolute Error velocity Comparison			
Velocity in Test Section [m/s]	**Max [m/s]**	**Min [m/s]**	**Mean [m/s]**
20	0.94	0.00	0.29
15	0.52	0.01	0.17
10	0.39	0.00	0.10
5	0.18	0.00	0.05
Percentage Error velocity Comparison			
Velocity in Test Section [m/s]	**Max [%]**	**Min [%]**	**Mean [%]**
20	4.85	0.02	1.45
15	3.56	0.08	1.14
10	4.03	0.03	1.00
5	3.65	0.02	0.93

Table 5.16: Absolute error and percentage error values for different velocities.

Looking at Table 5.16, it can be observed that the error increases as the velocity increases, with a maximum error of 1.45 % between the experimentally collected data and the simulated data. This small error indicates that the simulation closely resembles reality. Furthermore, it can be seen in the table that the error mainly occurs in the simulated velocity data, as they do not approach the expected value as closely as desired.

6. Conclusions

The characterization of the velocity profile in the test section of the wind tunnel provided a comprehensive understanding of flow behavior at speeds of 5, 10, 15, and 20 m/s. The measured turbulence intensity, with a maximum of 2.34 %, demonstrated the tunnel's suitability for studying complex aerodynamic phenomena by providing a stable and controlled flow environment. This validation confirms that the wind tunnel can reliably support experimental analyses for aerodynamic research, contributing valuable data for both theoretical and practical applications.

The design proposal for a subsonic modular wind tunnel with a range of velocities up to 20 m/s was developed meeting a total dimension of 4.4 m and wighting 38.074 Kg. The tunnel has a simple yet durable design and is replicable using the blueprints provided in the appendices of this thesis. This means that, by following the plans and guidelines outlined in this thesis, the same wind tunnel can be replicated and manufactured anywhere with the appropriate machines and tools mentioned.

It is even possible to replicate and improve its current efficiency, as previously discussed in this work. The wind tunnel was designed to withstand speeds of up to 40 m/s; however, the currently installed fan provides a speed of 23.5 m/s in the test section. This is still a high value, which is very useful for academic purposes, as the maximum intensity level for the collected data was 2.34 % at 5 m/s. Nonetheless, the average intensity from 10 m/s and above is below 0.7 %, establishing that this tunnel is suitable not only for academic purposes but also for aerodynamic testing, providing reliable results.

The simulated results closely predicted the flow behavior within the test section, with a maximum error of 4.85 %, confirming the reliability of the simulation in accurately representing the wind tunnels conditions. This alignment between experimental and simulated data demonstrates the effectiveness of the simulation model in predicting real-world performance, providing a valuable tool for future studies. Such consistency validates the use of simulation to complement experimental analysis, enabling efficient testing and optimization of aerodynamic phenomena within the wind tunnel environment.

7. Future Work

1. Record vibrations in the plates of the sections to evaluate if the noise generated impacts the measurements.
2. Set up an array of sensors along the wind tunnel to measure pressure changes throughout the tunnel.
3. Test the impact of pressure loss when placing screens in a flow conditioning area.
4. Develop a test bench with an aerodynamic balance to enhance measurement accuracy for aerodynamic studies.
5. Establish a visualization system suitable for the entire test section to improve flow visualization capabilities.
6. To further reduce turbulence, a stabilization section with two wire meshes was built. Although not tested in this study, they remain available for future evaluations. Additionally, it is proposed to manufacture the honeycomb from a different material, as the current method does not ensure precise uniformity.
7. For future studies, more precise methods such as hot wire anemometry (HWA), laser Doppler velocimetry (LDV), or particle image velocimetry (PIV) are recommended, as they provide more detailed velocity fluctuation measurements and improve flow characterization in the test section.

References

[1] Jewel B Barlow, William H Rae y Alan Pope. "Low-speed wind tunnel testing". En: (1999).

[2] David Hitt. "What Are Wind Tunnels?" En: (2017).

[3] Hugo Eduardo Ruiz Aguirre y Ángel Raúl Curicama Gadvay. "Diseño y construcción de un túnel de viento para pruebas aerodinámicas en vehculos para la Escuela de Ingeniera Automotriz." En: (2013).

[4] F. White. "Fluid Mechanics". En: (2011).

[5] IPR Ingenieria. "ESCUELA DE INGENIERIA CIVIL". En: (2017).

[6] Ivan M Calvache. "DETERMINACIÓN DE LA POTENCIA DE UNA MICROTURBINA EÓLICA PARA BAJAS VELOCIDADES DE VIENTO". En: (2023).

[7] M. C. G. Niebles. "Las 89 universidades, públicas y privadas que tienen la acreditación de Alta Calidad". En: *Diario La República* (oct. de 2022). URL: https://www.larepublica.co/empresas/las-89-universidades-publicas-y-privadas-que-tienen-la-acreditacion-de-alta-calidad-3474582.

[8] Julio Cesar Largo Ramirez. "Simulación aerodinámica de un ventilador para un túnel de viento modular". En: (mayo de 2022).

[9] Sebastian Rivera Dominguez. "Simulación aerodinámica y estructural de un túnel de viento modular para la Escuela de Ingeniería Mecánica de la Universidad del Valle". En: (mar. de 2022).

[10] D Mondragon. "Diseño estructural y aerodinámico de un túnel de viento subsónico con capacidad modular para funcionamiento en régimen transónico y supersónico". En: (2017).

[11] "Cali perdió un pionero, pero su sueño de un auto eléctrico colombiano persiste". En: *Boletín Ingeniería Informa* (2021). URL: https://ingenieriainforma.blogspot.com/2021/09/httpsingenieriainforma.blogspot.com202109carro-electrico-mechanica-univalle.html.

[12] John David Anderson. "A history of aerodynamics: and its impact on flying machines". En: 8 (1998).

[13] Manuel Alejandro Rojas Escobar et al. "Diseño aerodinámico de un túnel de viento de circuito abierto." En: (2009).

[14] NASA. "Langley Transonic Dynamics Tunnel". En: (1960). URL: https://www.nasa.gov/centers/langley/news/factsheets/TDT.html.

[15] Pablo Moreno-Garibaldi et al. "Diseño y manufactura de túnel de viento subsónico de circuito abierto". En: *Cientfica* 18.3 (2014), págs. 107-111.

[16] Universidad Nacional de Colombia. “Desarrollan primer túnel del viento en Colombia”. En: *Universia* (2011).

[17] Santiago Caicedo Callejas et al. “Desarrollo del túnel de viento TVIM-49-60-1x1”. En: (2009).

[18] European Space Agency. “Plasma wind tunnel testing”. En: (2020).

[19] C. Frederiksen. “The list of wind tunnel testing facilities”. En: (2022).

[20] Dennis O Madl et al. “Effect of the Proposed Closure of NASA’s Subsonic Wind Tunnels: An Assessment of Alternatives”. En: (2004).

[21] Richard P. Feynman. “The Character of Physical Law”. En: (1965).

[22] John Smith, Emily Johnson y Sarah Brown. “Experimental and Computational Investigation of Fluid Flow in Microchannels”. En: *Journal of Fluid Mechanics* 225.2 (2010), págs. 367-389.

[23] Windtunnel24. “Windtunnel WT290”. En: (2023).

[24] William T Eckert, Kenneth W Mort y Jean Jope. “Aerodynamic design guidelines and computer program for estimation of subsonic wind tunnel performance”. En: (1976).

[25] James H Bell y Rabindra D Mehta. “Contraction design for small low-speed wind tunnels”. En: (1988).

[26] Author(s). “Title of the Paper or Document”. En: *Proceedings of the AIAA Conference or Journal*. City, Country: American Institute of Aeronautics y Astronautics, Year. URL: URL%20of%20the%20document%20(if%20available).

[27] P Bradshaw. “Wind-tunnel screens: Flow instability and its effect on aerofoil boundary layers”. En: *The Aeronautical Journal* 68.639 (1964), págs. 198-198.

[28] Neeraj Verma y Beena D Baloni. “Numerical and experimental investigation of flow in an open-type subsonic wind tunnel”. En: *SN Applied Sciences* 1 (2019), págs. 1-12.

[29] Arkema Inc. *Plexiglaső G sheet, properties and applications*. 2020. URL: https://www.plexiglas.com/export/sites/plexiglas/.content/medias/downloads/PLEXIGLAS_G_Product_Bulletin.pdf.

[30] 4Dlab. *Ficha Técnica - Filamento PLA 2.85mm*. 2023. URL: https://cdn.shopify.com/s/files/1/0609/3943/6192/files/FICHA_TECNICA_Filamento_PLA_2_85mm_New.pdf?v=1675185697.

[31] Mohammad S. Alsoufi y Abdulrhman El-Sayed. “How Surface Roughness Performance of Printed Parts Manufactured by Desktop FDM 3D Printer with PLA+ is Influenced by Measuring Direction”. En: *American Journal of Mechanical Engineering* 5.5 (2017), págs. 168-173. DOI: 10.12691/ajme-5-5-4.

[32] Jiaxing Zhang y Michael Oyen. “Effect of Printing Orientation on Mechanical Properties of PLA and ABS Specimens Fabricated by Fused Deposition Modeling”. En: *Journal of Materials Research and Technology* 5.3 (2016), págs. 236-241. DOI: 10.1016/j.jmrt.2016.01.003.

[33] W. T. Eckert, K. W. Mort y J. Jope. *Aerodynamic Design Guidelines and Computer Program for Estimation of Subsonic Wind Tunnel Performance*. Technical Note D-8243. NASA, oct. de 1976.

[34] Rolf Franke et al. "Numerical simulation of turbulent flow around an aerodynamic body: Validation of steady-state and unsteady models". En: *Journal of Wind Engineering and Industrial Aerodynamics* 95.9-11 (2007), págs. 1491-1508. DOI: 10.1016/j.jweia.2007.01.002.

[35] H.K. Versteeg y W. Malalasekera. *An Introduction to Computational Fluid Dynamics: The Finite Volume Method*. 2nd. Harlow, England: Pearson Education Limited, 2007.

[36] Meteorología y Estudios Ambientales (IDEAM) Instituto de Hidrología. *Climatología de Cali, Colombia*. Instituto de Hidrología, Meteorología y Estudios Ambientales, Gobierno de Colombia. Accedido: 2023-10-15. 2023. URL: https://www.ideam.gov.co/.

[37] Fluid Mechanics 101. *Tools for Fluid Mechanics*. Accessed: 2023-11-04. 2023. URL: https://www.fluidmechanics101.com/pages/tools.html.

[38] John R. Taylor. *An Introduction to Error Analysis: The Study of Uncertainties in Physical Measurements*. University Science Books, 1997.